



저작자표시-동일조건변경허락 2.0 대한민국

이용자는 아래의 조건을 따르는 경우에 한하여 자유롭게

- 이 저작물을 복제, 배포, 전송, 전시, 공연 및 방송할 수 있습니다.
- 이차적 저작물을 작성할 수 있습니다.
- 이 저작물을 영리 목적으로 이용할 수 있습니다.

다음과 같은 조건을 따라야 합니다:



저작자표시. 귀하는 원저작자를 표시하여야 합니다.



동일조건변경허락. 귀하가 이 저작물을 개작, 변형 또는 가공했을 경우에는, 이 저작물과 동일한 이용허락조건하에서만 배포할 수 있습니다.

- 귀하는, 이 저작물의 재이용이나 배포의 경우, 이 저작물에 적용된 이용허락조건을 명확하게 나타내어야 합니다.
- 저작권자로부터 별도의 허가를 받으면 이러한 조건들은 적용되지 않습니다.

저작권법에 따른 이용자의 권리는 위의 내용에 의하여 영향을 받지 않습니다.

이것은 [이용허락규약\(Legal Code\)](#)을 이해하기 쉽게 요약한 것입니다.

[Disclaimer](#)

Ph. D DISSERTATION

플라즈마 디웨팅을 이용한 금속 나노분말 array
제조에 관한 연구

The new method for producing metal
nanoparticle arrays using plasma-induced
dewetting

Soon-Ho Kwon

February 2013

Department of Materials Science and Engineering

College of Engineering

SEOUL NATIONAL UNIVERSITY

Abstract

A new method of producing metal nanoparticle arrays was developed with the help of plasma-induced dewetting. Various metal films (Cu, Ag, Au, Si, Ni, Co, Ti) were successfully turned into nanoparticle arrays at low operating temperatures. The mechanism of the plasma-induced dewetting was also discussed. TEM and SEM images showed that the dewetting proceeded through heterogeneous hole nucleation mechanism.

The nanoparticles produced by plasma-induced dewetting were more uniformly distributed on the substrate than those produced by thermal annealing. It was revealed that low process temperature of the plasma treatment prevented coarsening of the nanoparticles, and uniformly distributed holes on the film surface, resulting in uniform nanoparticle arrays, were detected during plasma treatment.

According to AES (auger electron spectroscopy), oxidation of the nanoparticles occurred less during plasma treatment because of the low operating temperature. Even at the low temperature, ion bombardment which transfers high energy to the substrate surface atoms made dewetting possible.

The uniformity of nanoparticle arrays was controlled by varying plasma parameters. Plasma density and electron temperature were controlled by varying working pressure and applied RF power. Sheath voltage was also controlled directly using substrate bias. It was found

that uniform nanoparticle arrays were produced when hole generation was increased by using high ion bombardment energy. When a low amount of energy was transferred to the substrate, small numbers of holes were generated on the film surface, resulting in non-uniformly distributed nanoparticles.

Contents

1. Introduction
2. Research background and theory
 - 2.1 Dewetting of thin film
 - 2.1.1 Liquid thin film dewetting
 - 2.1.2 Solid–state dewetting of thin film
 - 2.1.2.1 Hole formation
 - 2.1.2.2 Hole growth
 - 2.2 Inductively coupled plasma
3. Experimental procedure
 - 3.1 Film deposition and post–treatment
 - 3.2 Analysis methods
4. Result and Discussions
 - 4.1 Formation of Cu nanoparticle arrays by plasma–induced dewetting
 - 4.2 The hole nucleation mechanism of the plasma–induced dewetting
 - 4.2.1 Surface morphology analysis with SEM
 - 4.2.2 TEM analysis
 - 4.2.3 AFM analysis

- 4.2.4 SLP analysis
- 4.3 Uniformity control of nanoparticle arrays
 - 4.3.1 Process temperature effect
 - 4.3.2 Ion bombardment energy effect
- 4.4 Various metal nanoparticle arrays produced by plasma-induced dewetting
 - 4.4.1 Low melting temperature metals
 - 4.4.2 High melting temperature metals
- 5. Conclusion

List of Figures

Figure 1–1. Schematic diagram of surface plasmon.

Figure 1–2. (a) The Cu nanoparticle array and (b) single wall carbon nanotube using Cu nanoparticle as a catalyst.

Figure 1–3. Schematic diagram of nano–floating gate memory.

Figure 2–1. Schematic diagram of dewetting of thin film.

Figure 2–2. The diagram of the effective interface potential $G(h)$ as a function of film thickness for (1): stable, (2): unstable and (3) metastable film.

Figure 2–3. The figure showing why a molecule in a thin film is attracted toward the thicker parts of the thin film. M indicates a molecule.

Figure 2–4. Fourier component of the perturbation of a thin film of average thickness, h_0 .

Figure 2–5. The equilibrium shape of a nanoparticle with an isotropic surface energy on a rigid substrate. γ_f , γ_i and γ_s are the surface energy of the nanoparticle, the energy of the nanoparticle–substrate interface and the surface energy of the substrate, respectively.

Figure 2–6. Schematic cross–sectional view of polycrystalline film' s grain boundary area. The grain diameter is $2R$, the film thickness is a , and the equilibrium groove depth is d .

Figure 2–7. Hole nucleation image of (a) Au, (b) Pt, (c) Cu film.

Figure 2–8. Schematic of inductively driven sources in (a) cylindrical and (b) planar geometries.

Figure 2–9. Schematic of the mechanism of discharge by the induced electric field inside the coil

Figure 3–1. Schematic diagram of DC sputtering system

Figure 3–2. Schematic diagram of post–treatment chamber

Figure 3–3. Schematic diagram of substrate bias part of post–treatment chamber

Figure 3–4. Image of the thermal tape which is attached on the substrate.

Figure 3–5. I–V characteristic for a single Langmuir probe. A : electron saturation region, B: electron retardation region and C: ion saturation region.

Figure 4–1 Cu nanoparticles after 500 W Ar plasma treatment for 1 h at 20 mT. The operating temperature was 450 K. The thicknesses of the Cu films were (a) 1 nm, (b) 2 nm, (c) 4 nm, (d) 6 nm and (e) 8 nm. Notice that (a) has a different scale bar. (f) Dependence of the average diameter of Cu nanoparticles as a function of theas–deposited Cu film thickness.

Figure 4–2. UV–vis spectroscopy measurement data of the various Cu nanoparticle arrays.

Figure 4–3. SEM images of Cu nanoparticles on polyimide (PI) substrate after (a) 300 W and (b) 500 W Ar plasma treatment for 10 min at 20 mT.

Figure 4–4. SEM images of Cu nanoparticles on polyimide (PI) substrate after 300 W Ar plasma treatment for (a) 10 min and (b) 30 min at 20 mT.

Figure 4–5. Schematic diagram of ion bombardment on substrate surface. Only the film surface atoms become mobile.

Figure 4–6. SEM images of 5 nm Cu films after 750 W Ar plasma treatment at 20 mT for different times: (a) as–deposited film, (b) 1 min, (c) 1.5 min, (d) 2 min, (e) 2.5 min and (f) 10 min.

Figure 4–7. FE–SEM images of 5 nm Cu films after 750 W Ar plasma treatment at 20 mT for different times: (a) as–deposited film, (b) 20 s,

(c) 30 s, (d) 40 s, (e) 50 s, and (f) 10 min. Note that (f) has a different scale bar.

Figure 4–8. HR–TEM images of as–deposited 5 nm Cu film. Note that (a) and (b) have different scale bars.

Figure 4–9. Cross–sectional TEM images of Cu films: (a) as–deposited film and (b) after Ar plasma treatment for 40 s. (figure 4–7 (d) sample)

Figure 4–10. Diffraction image of 5 nm Cu thin film.

Figure 4–11. AFM image of the Cu film: (a) the surface image and (b) the height curve in the cross–sectional direction.

Figure 4–12. Image of a two–dimensional Fourier transform data

Figure 4–13. SEM images of the 4 nm Cu/SiO₂ samples after heat treatment with H₂ gas for 2 h at (a) 473, (b) 573 and (c) 773 K. Note that (b)–2 has a different scale bar. The images of (b)–1 and (b)–2 are for same sample.

Figure 4–14. SEM images of the Cu/SiO₂ samples after the 500 W Ar plasma treatment for 1 h at 20 mT. The operating temperature was 450 K. The thickness of the Cu films was (a) 4 nm and (b) 8 nm. The same images were shown in figure 4–1.

Figure 4–15. SEM images of the Cu/SiO₂ samples after the 500 W H₂ plasma treatment for 1 h at 20 mT. The operating temperature was 420 K. The thickness of the Cu films was (a) 4 nm and (b) 8 nm.

Figure 4–16. SEM images of the 4 nm Cu/SiO₂ samples after the 500 W plasma treatment in (a) H₂ and (b) Ar at 773 K for 1 h.

Figure 4–17. AES data of (a) thermally annealed 4 nm Cu film and (b) Ar plasma treated 4 nm Cu film on Si substrate.

Figure 4–18. SEM images of the 4 nm Cu/Si samples after (a) the 573 K annealing and (b) the 500 W plasma treatment for 30 min.

Figure 4–19. FE–SEM images of 5 nm Cu films (a) after heat treatment with H₂ gas for 1 min at 653 K and (b) after 750 W Ar plasma treatment for 1 min. The plasma treatment condition of (b) was the same as figures 6 and 7.

Figure 4–20. FE–SEM images of Cu nanoparticle arrays after Ar plasma treatment for 1 hour. The operating pressures were (a) 20 mTorr and (b) 100 mTorr.

Figure 4–21. FE–SEM images of 4 nm Cu film after the Ar plasma treatment at 20 mTorr: (a) 30 S, (b) 1 min and (c) 2 min.

Figure 4–22. FE–SEM images of 4 nm Cu film after the Ar plasma treatment at 100 mT for: (a) 30 S, (b) 1 min and (c) 2 min.

Figure 4–23. FE–SEM images of Cu nanoparticles array after 1 hour Ar plasma treatment at 100 mT and 190 W. Induced self–DC bias on the substrate was –50 V.

Figure 4–24. FE–SEM images of Cu nanoparticles array after 1 hour Ar plasma treatment. The operating pressures was 20 mTorr. Induced RF powers were (a) 750 W and (b) 400 W.

Figure 4–25. FE–SEM images of the 5 nm Al/SiO₂ samples; (a) as–deposited sample, (b) after 12 hours 700 W Ar plasma treatment, (c) after 12 hours 700 W H₂ plasma treatment.

Figure 4–26. FE–SEM images of the 5 nm (a) Au/SiO₂ and (b) Ag/SiO₂ samples after 500 W Ar plasma treatment for 30 min.

Figure 4–27. FE–SEM images of Au films after the 750 W Ar plasma treatment for different times: (a) as–deposited film, (b) 1 min, (c) 2 min, (d) 3 min, (e) 5 min, and (f) 30 min. Note that (f) has a different scale

bar.

Figure 4-28. FE-SEM images of the 5 nm (a) Si/SiO₂, (b) Ti/SiO₂, (c) Ni/SiO₂ and (d) Co/SiO₂ samples after Ar plasma treatment for 2 hours using substrate bias. Note that (c) and (d) has a different scale bar with (a) and (b).

List of Tables

Table 4-1. Plasma parameter of figure 4-20 experimental condition

Table 4-2. Plasma parameter of figure 4-20 experimental condition.

1. Introduction

Metal nanoparticle arrays are used in various applications, such as device using surface plasmonic resonance properties, sensor, metal nanocrystal memory, solar cell, storage media, light emitting diode display, seeds of nanostructure and ferromagnetic applications.[1–18]

1) Application using localized surface plasmon resonance property

Surface plasmon means collective charge density fluctuation at a metal/dielectric interface, excited by light and bound to the surface (figure 1–1). Surface plasmon can couple into radiation when momentum conservation is satisfied on the surface via a periodic structure or nano-scale roughness. The surface plasmon resonates with the light which has specific wave length. Therefore, absorbance peak is observed in the specific wave length when the sample showing plasmon property is analyzed by UV–vis spectroscopy. The absorbance peak can be modified by controlling the sample condition. Using the absorbance peak shift, various chemical reactions or selective dissociation and combination between biochemical materials can be detected precisely. Therefore, it has been used in biosensor field. Moreover, plasmon resonance property is used for increasing photo-absorbance efficiency of solar cell by applying the specific wave length absorbance layer. In metal nanoparticle array, the surface plasmon resonance property is observed intensively. The surface plasmon resonance on the metal nanoparticle is called localized surface plasmon resonance (LSPR). By controlling the size of nanoparticles, the absorbance peak can be modified. Therefore, in these

days, research of various metallic nanoparticle arrays, such as Ag, Au, Cu nanoparticle arrays, become a hot issue.

2) Seed layer of nanostructure

Metal nanoparticle array is essential for producing nanostructure, such as nanowire and nanorod, because of its catalytic property. Especially, Co, Ni, Au and Cu are usually used for the catalyst of nanostructure (figure 1-2). Because the property of nanostructure is heavily influenced by size and uniformity of the metal nanoparticle array and processing temperature during synthesizing the catalyst, controlling nanoparticle within the constraint of the application condition is a very important issue. For example, Cu nanoparticle array have an advantage with growing ZnO nanowire on the Si substrate because Si-Cu have high eutectic point (802 ° C) [10, 19]. If Au is used for the catalyst of ZnO nanowire, Au-Si alloy formed rapidly on the substrate because of their low eutectic point [19]. It results in degradation of ZnO nanowire. Decreasing reaction between metal nanoparticle array and substrate can be achieved by lowering process temperature.

3) Nano-floating gate memory

Nano-floating gate memory is the memory in which nanoparticle arrays, such as Ag, Ag and Cu, are used as an electron trapper, whereas thin film is used in conventional transistor. The nano-floating gate memory device is not influenced by damage of tunneling oxide layer and the thickness of tunneling layer can be minimized. Therefore, the device is faster and more reliable than conventional transistor. In the nano-floating gate memory, uniformity of the metal nanoparticle is very important and low temperature process is needed.

The metal nanoparticle arrays, below 100 nm particle size, have been produced through numerous methods, including lithography using electron-beam, x-ray, extreme UV and SPM (Scanning Probe Microscope), nano-imprinting lithography, metal transfer printing, self-assembly monolayer, nanotransfer molding, chemical reaction method using a copolymer solution and dewetting using thermal annealing and pulsed-laser [20–37]. Among these, there are a few methods that do not use organic materials during process. Since organic materials result in pollution of metal nanoparticle arrays, avoiding organic materials during the process is very important in many applications. A typical method which does not use organic materials is dewetting of thin film. Of course other organic-free methods also exist, but methods which the target materials are processed into nanoparticle arrays are limited [38]. Among dewetting methods, thermal annealing is most widely used because the process is relatively simple and low cost. Moreover, reaction of metal particles with substrate materials could be reduced when the process is carried out in solid state. However, nanoparticles produced by thermal annealing are not uniformly distributed compared to other dewetting methods, and long processing time is needed for high melting point metal nanoparticles, such as Si and Ti. The liquid-state dewetting by pulsed laser ablation can induce spinodal dewetting if the film thickness is controlled. By spinodal dewetting, more uniformly distributed nanoparticles can be formed. The shortcoming of the laser method, however, is the high process temperature and high production cost.

For various applications, it is important to develop a new dewetting process satisfying the following terms: low temperature, low-cost,

scalable, capable of processing various materials and controlling nanoparticle size.

1) Dewetting in solid-state is essential in order to low temperature process. For now, solid-state dewetting is processed by thermal annealing, and, in most cases, process temperature above 300 °C is needed for forming completely dewetted nanoparticle arrays. Therefore, it is hard to use the polymer substrate which is necessary to various applications. For example, polycarbonate (PC) and polyimide (PI) can endure until 200 °C and 300 °C, respectively. Therefore, a new synthesizing method for nanoparticle arrays which is processed at lower temperature is needed. Furthermore, low process temperature process also has an advantage on reducing oxidation of metal nanoparticles.

2) The new nanoparticle array producing method has to be promising way for mass production.

3) The new method should be capable of processing various metals. Because of characteristic of metals, diverse metal nanoparticle arrays are needed for various applications. For example, Co nanoparticle arrays are used for magnetic application. Co, Ni, Au and Cu is essential for seed of nanostructure, and Au, Ag, Al, Si, Cu is needed for plasmonic applications.

4) The size and uniformity of metal nanoparticle should be controlled for applications. For example, the wave length in which surface plasmon resonance is occurred can be modified if the control of size and uniformity of nanoparticles are possible.

To achieve these goals, inductively coupled plasma (ICP) was

introduced in this study. ICP has been used as an activation source for lowering the substrate temperature and enhancing plasma density [39]. Moreover, ICP has already been used for etching process in mass production. Using these advantages, various metal nanoparticle arrays were produced while satisfying the essential conditions. In plasma-induced dewetting, the process temperature was lower than thermal annealing, and the size and uniformity of nanoparticle was controllable. The effect of low temperature process and mechanism of plasma-induced dewetting were also revealed.

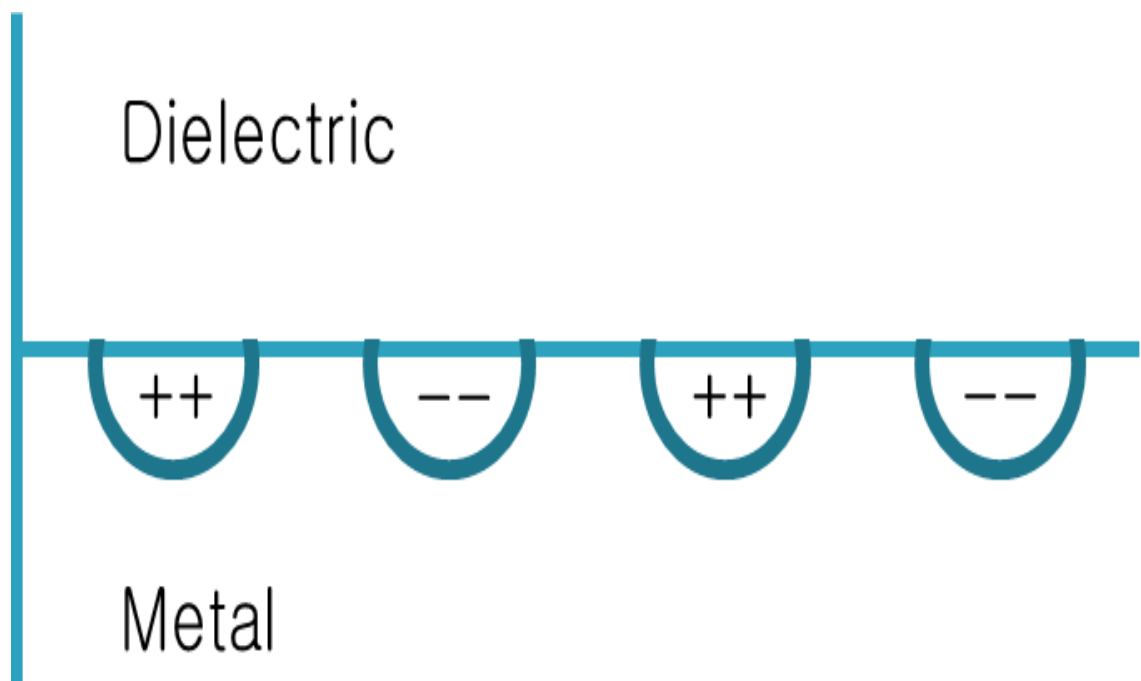
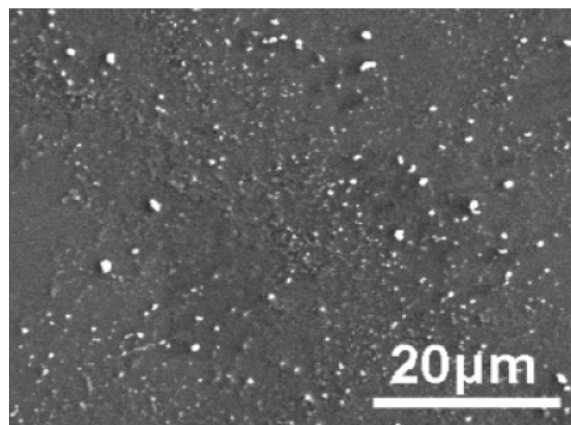
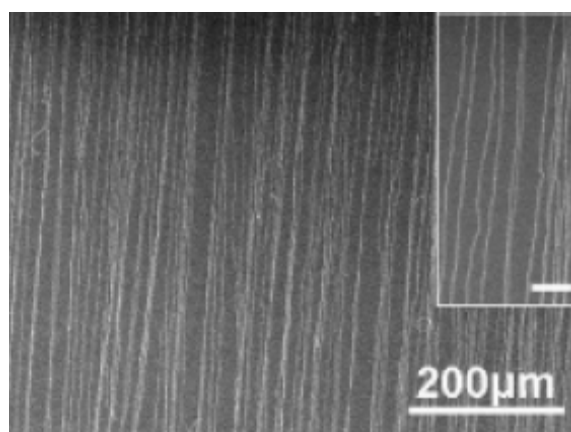


Figure 1-1. Schematic diagram of surface plasmon



(a)



(b)

Figure 1–2. (a) The Cu nanoparticle array and (b) single wall carbon nanotube using Cu nanoparticle as a catalyst [8].

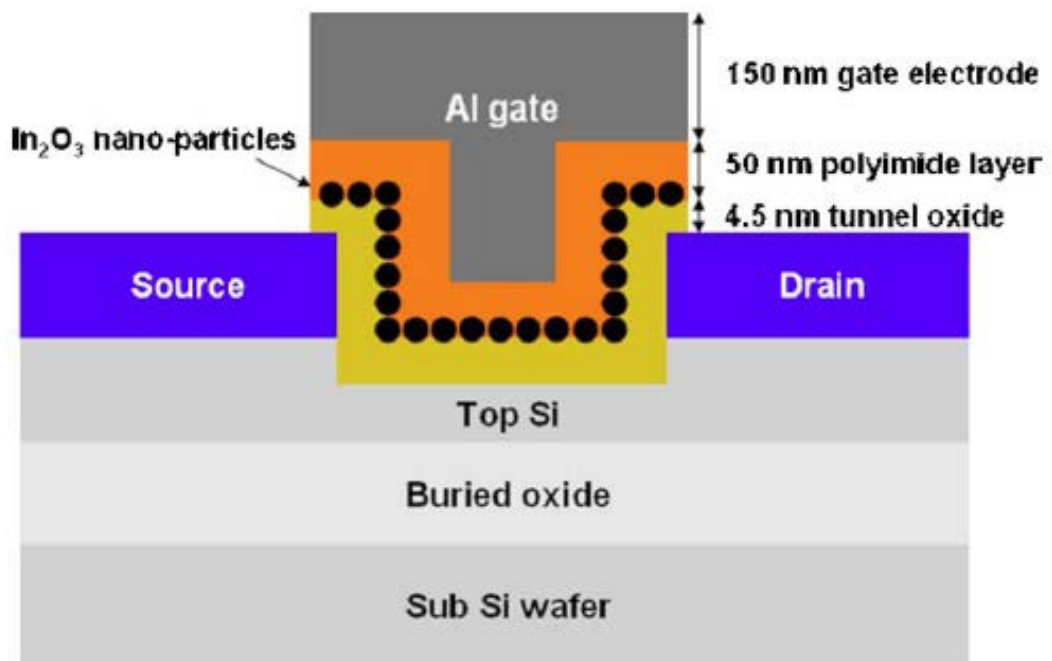


Figure 1-3. Schematic diagram of nano-floating gate memory

2. Research background and theory

2.1 Dewetting of thin film

2.1.1 Liquid thin film dewetting

Originally, dewetting of thin film is one of the processes that can occur at a liquid film on solid or liquid substrate [40, 41]. The dewetting describes the rupture of a thin liquid film on the substrate (either a liquid itself, or a solid) and the formation of droplets (figure 2-1). Therefore, it is important to explain the liquid-state dewetting for understanding the solid-state dewetting process. Basically, the driving force for dewetting is minimization of the total energy of the free surface of the film and substrate. Hence, expressing Gibbs energy, ΔG , as a formula is important.

Owing to the simplicity of the model system of a thin film (<60 nm) of liquid film on solid substrate, it is possible to calculate the effective interface potential, $G(h)$; h is the film thickness [42, 43]. With $G(h)$, 3 cases of the film state can be considered as shown in figure 2-2; stable, unstable and metastable.

Curve (1) describes a state where $G(h) > 0$, where global minimum of $G(h)$ lies at infinite film thickness. In this case, the thin film is stable.

In Curve (2), which indicates unstable state, a global minimum is at $h'=0$. If the initial film thickness is thicker than h at $h'=0$, the film will dewet because the thinner film (h at $h'=0$) is more stable. In unstable region, three types of rupture of thin film are possible, heterogeneous nucleation, thermal nucleation and spinodal dewetting. In heterogeneous

nucleation, defect on the film surface becomes hole nucleation site. If thermal activation is sufficient to overcome the potential barrier for nucleation of a defect, it is called thermal (hole) nucleation [44]. The last one, spinodal dewetting, can be expressed as mathematical expressions. When the film is very thin (<60 nm), the fluctuations in the two surfaces become correlated because of the molecular interactions in the film. Van der Waals forces are always present and tend to drive the molecules from thinner to thicker parts of the film. As shown in figure 2–3, if we consider a molecule in film, in which the thickness increases to right, the attraction by left part from M is compensated by the mirror images of that part of the film; left and right parts of the M is also molecules of the film, of course. Therefore, remained right part molecules (dark area in figure 2–3) attract M to right. It means that Van der Waals forces enhance the perturbation of the film.

Opposite to Van der Waals force, the existence of a surface tension tends to make the surface of the film as flat as possible against the perturbation. Therefore, it is conceivable that the increase in surface Gibbs energy will be compensated by the total decrease in Van der Waals energy.

Now, we consider an area of the film of 1 nm long and Λ cm wide with a deformation as drawn in Figure 2–4, which is one of the many Fourier components into which the total perturbation of the film can be split up.

The Gibbs energy, ΔG , contained in this particular wave, compared to a completely flat film of thickness, h_0 , can be expressed as

$$\Delta G = \text{extra area} \times \gamma + \text{extra interaction energy}$$

(eq. 2.1)

Where γ is the surface tension. The extra area on the two sides of the film is given by

$$2 \int_{y=0}^{y=\Lambda} \left\{ \sqrt{[(dz)^2 + (dy)^2]} - dy \right\} =$$

$$2 \int_0^\Lambda \left[\sqrt{1 + \left(\frac{dz}{dy}\right)^2} - 1 \right] dy = \int_0^\Lambda \left(\frac{dz}{dy}\right)^2 dy \quad (\text{eq. 2.2})$$

If $G(h)$ is the Gibbs energy of interaction per unit area among all the molecules in the film, the extra interaction energy in the wave form of figure 2-4 is given by

$$\int_0^\Lambda \left[\frac{dG(h)}{dh} \Delta h + \frac{1}{2} \frac{d^2G(h)}{dh^2} (\Delta h)^2 \right] dy \quad (\text{eq. 2.3})$$

in which $\Delta h = h - h_0$

Since $z = z_0 + B \sin(2\pi y/\Lambda)$ and $h = h_0 + 2B \sin(2\pi y/\Lambda)$, the total extra Gibbs energy becomes

$$\begin{aligned}
\Delta G = \gamma \int_0^\Lambda \left(\frac{dz}{dy} \right)^2 dy + \int_0^\Lambda \frac{dG}{dh} 2B \times \\
\sin\left(\frac{2\pi y}{\Lambda}\right) dy + \frac{1}{2} \int_0^\Lambda \frac{d^2 G}{dh^2} 4B^2 \left(\sin\left(\frac{2\pi y}{\Lambda}\right) \right)^2 dy = \\
\gamma B^2 \frac{4\pi^2}{\Lambda^2} \int_0^\Lambda \left(\cos \frac{2\pi y}{\Lambda} \right)^2 dy + 0 + 2B^2 \frac{d^2 G}{dh^2} \int_0^\Lambda \left(\sin \frac{2\pi y}{\Lambda} \right)^2 dy \quad (\text{eq. 2.4})
\end{aligned}$$

if the total Gibbs energy is negative, this particular fluctuation will grow. It can be expressed as

$$\gamma B^2 \frac{4\pi^2}{\Lambda^2} + 2B^2 \frac{d^2 G}{dh^2} < 0 \quad (\text{eq. 2.5})$$

Or

$$\Lambda > \Lambda_{crit} = \sqrt{[-2\pi^2\gamma/(d^2 G/dh^2)]} \quad (\text{eq. 2.6})$$

In most cases, film width Λ is very long ($\Lambda \gg h_0$). Therefore, first term of eq. 1.5 becomes 0. When $G''(h) < 0$, perturbation of thin film tend to grow and, finally, it becomes break down. This dewetting mechanism is called 'spinodal dewetting'. Because the spinodal dewetting is processed by periodic fluctuation, uniformly distributed nanoparticles can be produced.

Curve (3) indicates metastable state. In this region, the film is unstable for small film thicknesses. Dewetting of thin liquid film only occurred in specific region (thickness between h at $h'=0$).

2.1.2 Solid–state dewetting of thin film

In solid–state thin films, unstable or metastable condition in which dewetting occurs is satisfied in specific substrate and film system. As shown in figure 2–5, energy minimization gives the Young–Laplace equation, [45]

$$\gamma_s = \gamma_i + \gamma_f \cos \theta \quad (\text{eq. 2.7})$$

where γ_f , γ_i , γ_s and θ are the surface energy of the nanoparticle, the energy of the nanoparticle–substrate interface, the surface energy of the substrate and the equilibrium contact angle, respectively.

Only in $\gamma_f + \gamma_i > \gamma_s$ condition, the film will dewet when the rates of the necessary kinetic processes are sufficiently high. In the most applications, the substrate is usually oxide or polymer materials. Therefore, almost metal film is possible to dewet.

If dewetting condition is satisfied, solid–state thin film dewet through following sequence; hole formation and growth.

2.1.2.1. Hole formation

According to Mullins [46], the planar surfaces with isotropic surface

energies are stable with respect to all perturbations with amplitudes less than the film thickness. Consequently, an defect-free film dewet only when perturbation with large amplitude is applied (homogeneous hole nucleation mechanism). Because flat surfaces are stable with respect to small perturbation, a process that leads to hole formation is needed for dewetting with relatively small energy supply.

In polycrystalline film, grain boundaries and triple junction play important rule in hole formation. [47] To analyze effect of grain boundary in dewetting, D. J. Srolovitz et al. make two assumptions. The first is that at equilibrium, the angle between the grain boundary and the free surface is the equilibrium notch angle. The second is that the shape with a circular base and minimum surface area is a spherical cap. Therefore, the minimum energy surface shape is the spherical shape as shown in figure 2-6.

θ can be given by

$$\theta = \sin^{-1}\left(\frac{\gamma_{\text{grainboundary}}}{2\gamma_f}\right) \quad (\text{eq. 2.8})$$

Assuming conservation of film volume, an equilibrium groove depth, d , given by

$$d = R \frac{(2 - 3 \cos \theta + \cos^3 \theta)}{3 \sin^3 \theta} \quad (\text{eq. 2.9})$$

This grain boundary groove goes to a finite depth even after an infinite time process, such as annealing. Therefore, it is possible to calculate the conditions under which the groove intercepts the substrate. A film thickness a will rupture if

$$\left(\frac{R}{a}\right) \geq \frac{3 \sin^3 \theta}{2 - 3 \cos \theta + \cos^3 \theta} \quad (\text{eq. 2.10})$$

Therefore, grain boundaries satisfying above condition are possible to hole nucleation site. Especially, hole nucleation will be most likely at high-energy grain boundaries, small γ_f and h conditions and large γ_{gb} and R conditions. Moreover, in the actual process, sufficient energy transferred to the film is needed even if surface energy and angle at the grain boundaries satisfy dewetting condition, because the processing time cannot be infinite.

Srolovitz also researched grain boundary triple junctions. They showed that the grain boundary triple junctions provide the sites at which holes were nucleated most likely to form first. Moreover, other surface defects can be site of hole nucleation. It is called heterogeneous hole nucleation. However, as mentioned above, high amplitude energy can induce the homogeneous hole nucleation.

2.1.2.2 Hole growth

After hole formation, capillary energy drive retraction of its edge and the hole grow. The dominant atom transport mechanism in hole growth is diffusion process. In thermal annealing, the dewetted areas that

are growing from holes are sparse and separated by distances greater than the grain size as shown in figure 2-7 [48]. This is consistent with the research that the holes are not nucleated in all grain boundaries and the growth rate of hole is different in case by case because of the variation of grain boundary energies.

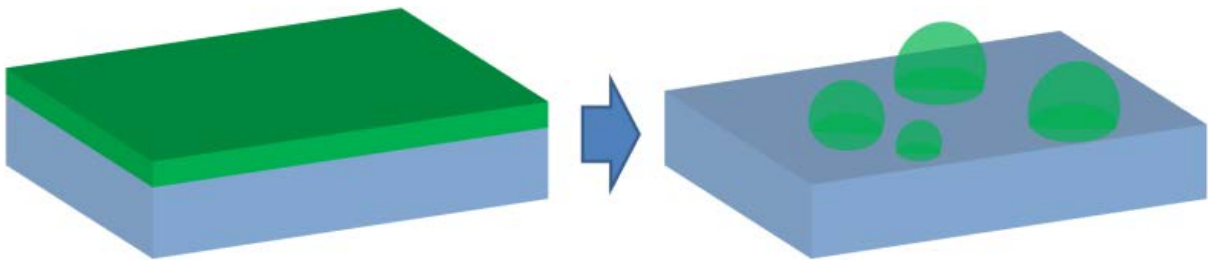


Figure 2-1. Schematic diagram of dewetting of thin film

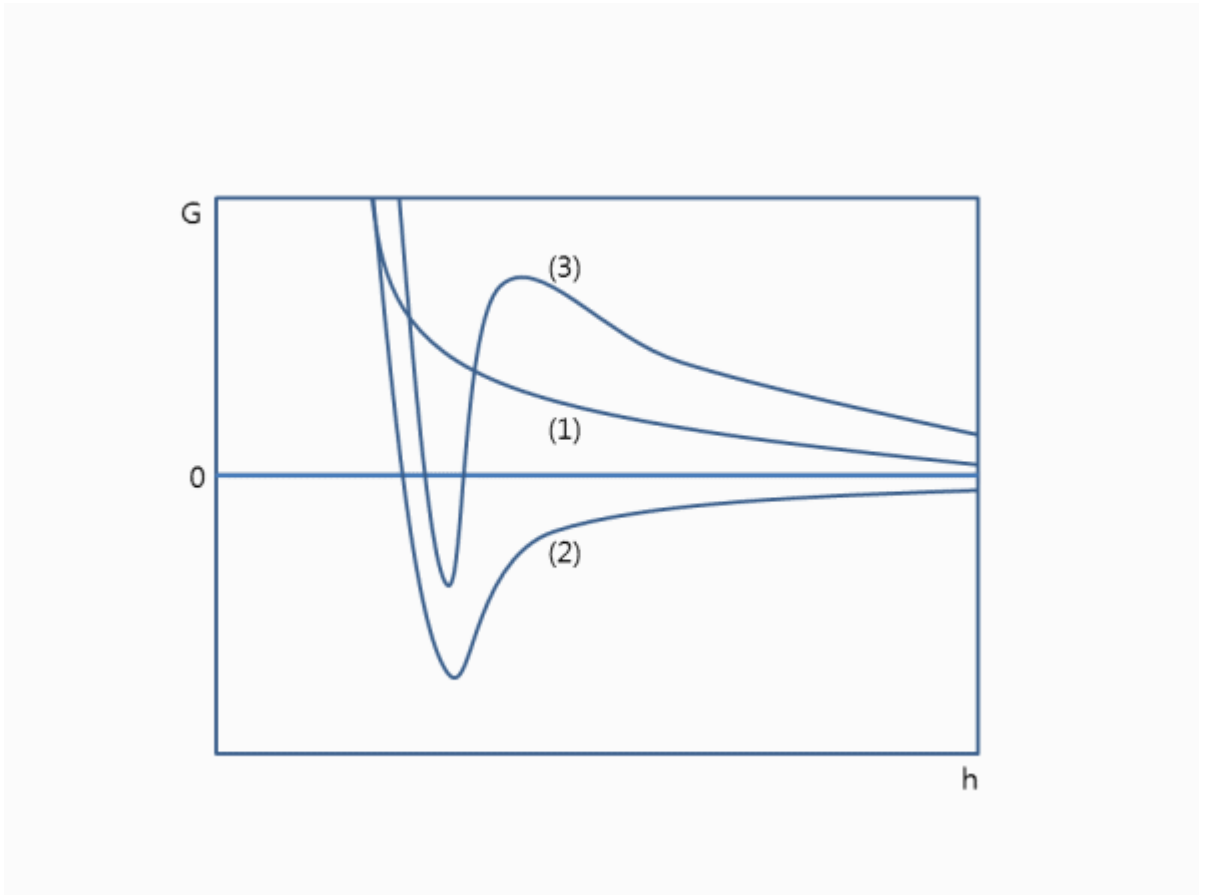


Figure 2-2. The diagram of the effective interface potential $G(h)$ as a function of film thickness for (1): stable, (2): unstable and (3) metastable film.

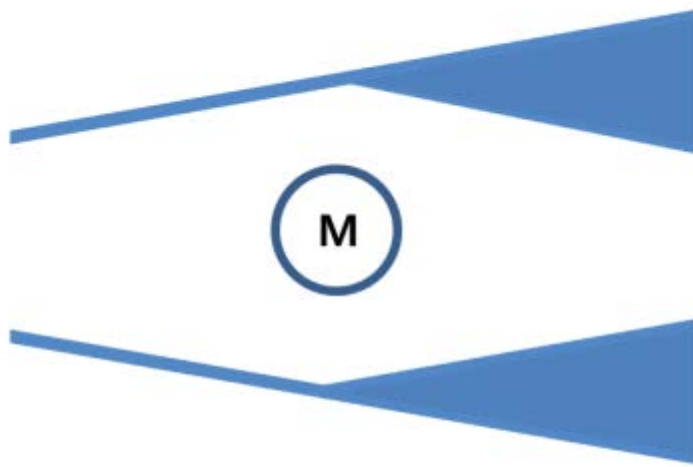


Figure 2–3. The figure showing why a molecule in a thin film is attracted toward the thicker parts of the thin film. M indicates a molecule.

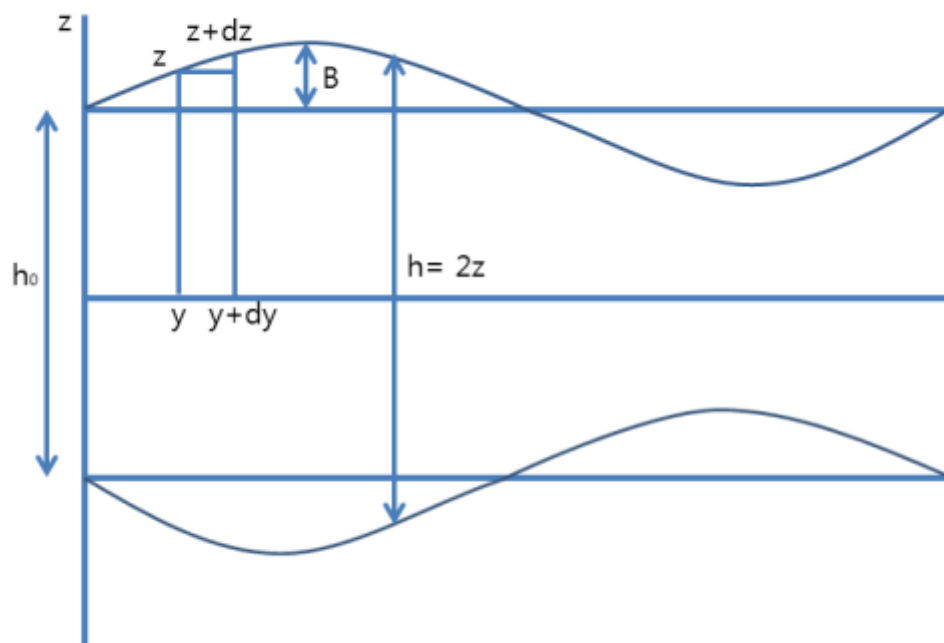


Figure 2-4. Fourier component of the perturbation of a thin film of average thickness, h_0 .

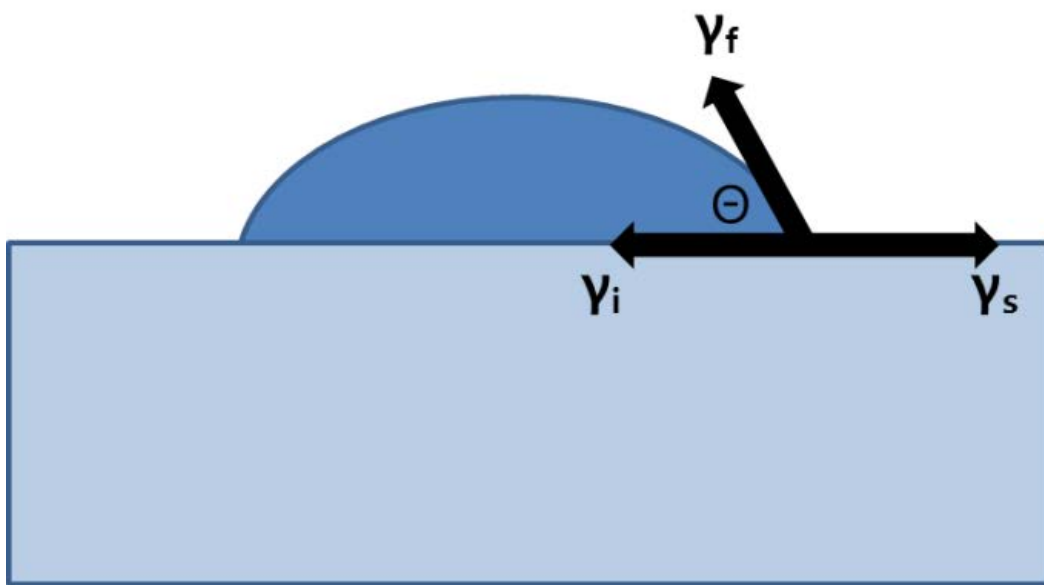


Figure 2–5. The equilibrium shape of a nanoparticle with an isotropic surface energy on a rigid substrate. γ_f , γ_i and γ_s are the surface energy of the nanoparticle, the energy of the nanoparticle–substrate interface and the surface energy of the substrate, respectively.

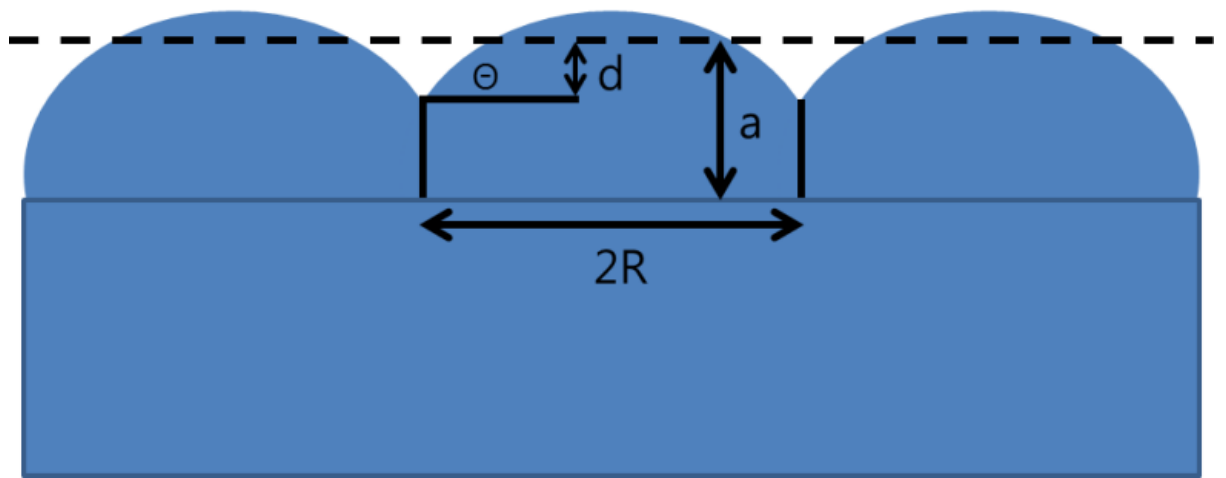
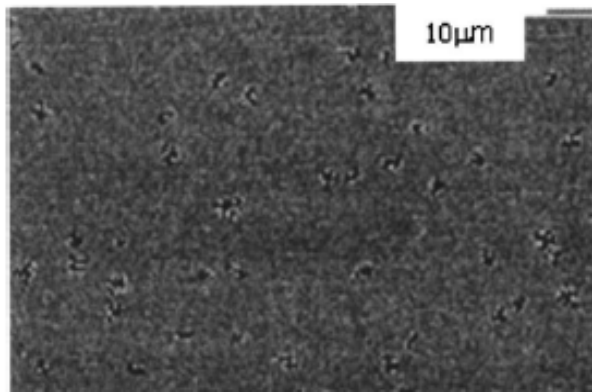
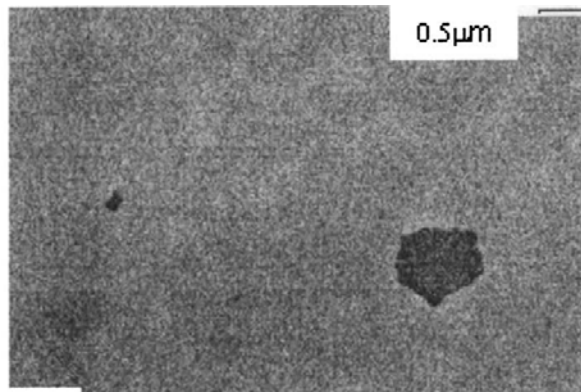


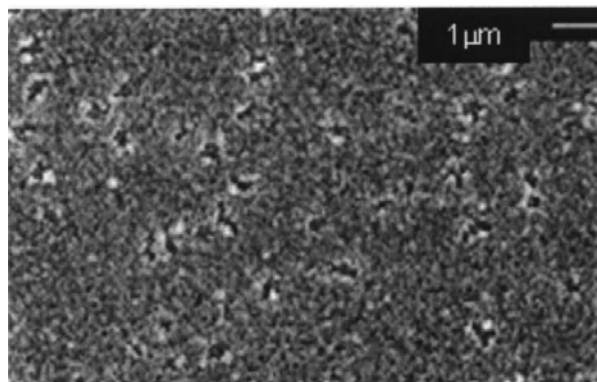
Figure 2-6. Schematic cross-sectional view of polycrystalline film's grain boundary area. The grain diameter is $2R$, the film thickness is a , and the equilibrium groove depth is d .



(a)



(b)



(c)

Figure 2-7. Hole nucleation image of (a) Au, (b) Pt, (c) Cu film [48].

2.2 Inductively coupled plasma

The limitation of conventional rf plasma led to the development of low-pressure and high density plasma discharges. The capacitively coupled plasma (CCP) has been widely used for plasma enhanced physical vapor deposition (PEPVD), plasma enhanced chemical vapor deposition (PECVD) and treatment of samples. In CCP, it is hard to increase plasma density up to 10^{11} cm^{-3} . Especially, in CCP, plasma density could not be high in low pressure because ionization frequency is proportional to the pressure. High density plasma is needed in many applications because it leads to the effective dissociation of precursor in CVD and it is a key factor of film quality in deposition process. High density plasma also has an advantage on treatment of sample surface, such as an etching process.

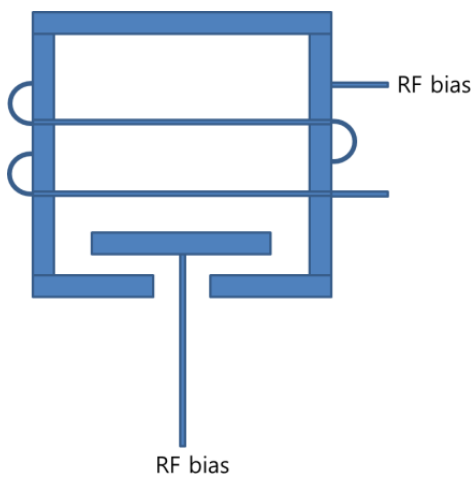
As one of the high density plasma sources, inductively coupled plasma was introduced by Hittorf in 1884. He wrapped a coil around an evacuated tube and observed a discharge when the coil was excited with a Leyden jar. After this research, many researches were done to identify whether this type of discharge were capacitively driven by plasma coupling to the low and high voltage ends of the cylindrical coil or were driven by the induced electric field inside the coil [49]. This issue was resolved that the discharge mode of plasma was transition to inductive mode (H-mode) with high plasma density from capacitive mode (E-mode) with low plasma density. Inductively driven sources in the cylindrical coil geometry and planar geometry (figure 2-8) were developed for low pressure application ($<50 \text{ mTorr}$). Plasma in the both

chambers is driven by externally placed coil. Driven plasma is present only where there is an rf electrical field. As shown in figure 2-9, the rf electric field inside the coil is induced by the time rate of change of the magnetic fields. Moving toward the center of the plasma chamber, the plasma current causes rf magnetic field, B_{rf} , opposite to that induced by the coil. Because of the penetration of magnetic field, the chamber using externally placed coil like figure 2-8 has to use the dielectric material, such as quartz plate, as the wall or the lid of the chamber.

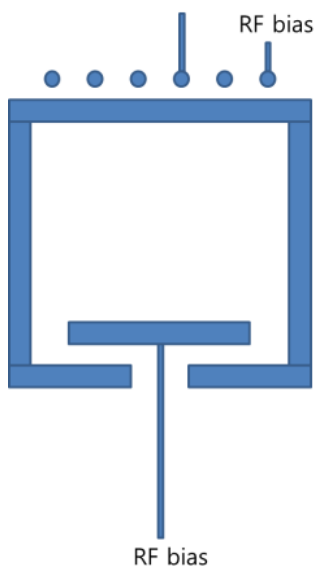
In deposition process, external ICP system is inappropriate because of the dielectric wall. Once target material or residues resulted by the gas reaction deposited on the dielectric wall, power generated by rf could not be transferred into the chamber. Therefore, dielectric wall should be cleaned frequently. Because of this inefficiency, internal ICP coil is needed for deposition process. However, internal ICP coil could be resulted in contamination of the substrate.

Given that the film contamination should be prevented and there is no possibility of material deposition on the dielectric wall, external ICP system will be appropriate for the dewetting process.

Using ICP, low electron temperature plasma can be obtained as well as high density plasma. Low electron temperature is resulted in the low sheath potential and it can be used in reducing the substrate damage. Therefore, ICP system will show advantage in dewetting process.



(a)



(b)

Figure 2–8. Schematic of inductively driven sources in (a) cylindrical and (b) planar geometries.

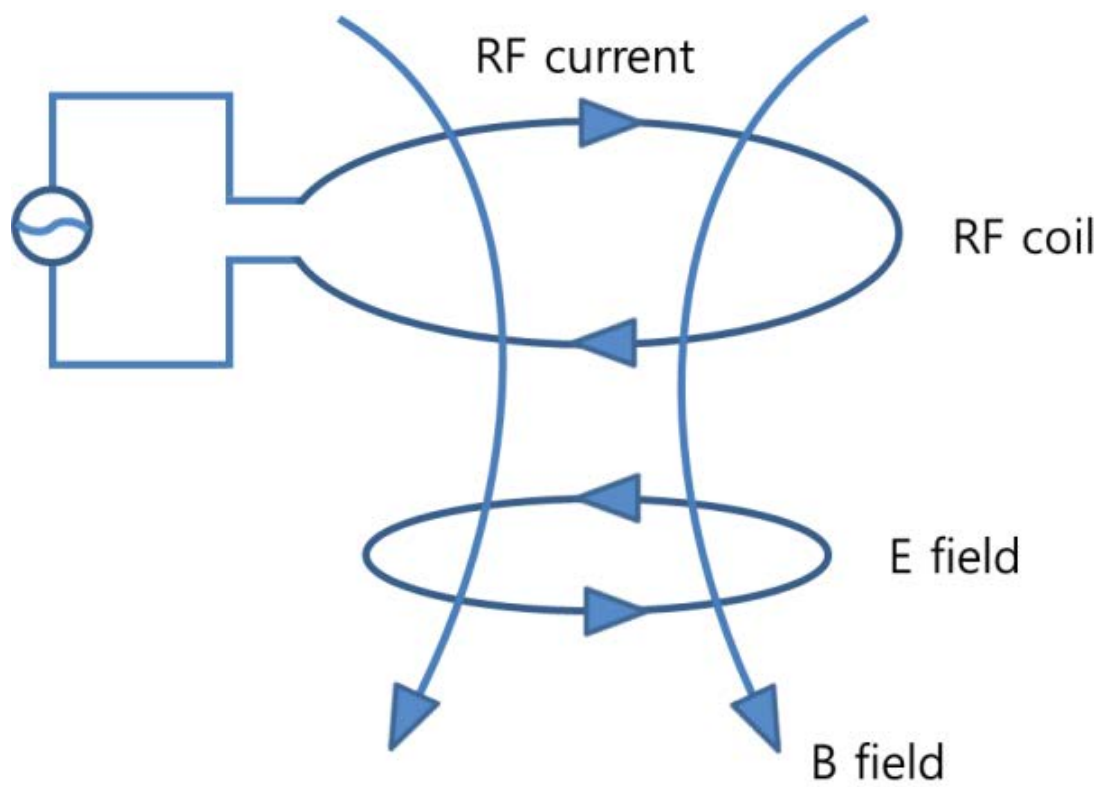


Figure 2-9. Schematic of the mechanism of discharge by the induced electric field inside the coil

3. Experimental procedure

3.1 Film deposition and post-treatment

Some research groups have reported that a stress-induced dewetting process achieved the formation of self-organized arrays of particles [50–52]. They showed that nanoparticles could be synthesized in a specific crystallographic system by the induced epitaxial strain between the substrate and film. In this research, amorphous SiO₂ was used as substrate to get rid of epitaxial strain factor during dewetting process. Moreover, amorphous SiO₂ was the most frequently used material as the substrate of the metal nanoparticle array. Therefore, various metal thin films were deposited onto amorphous SiO₂ substrate. Cu film was deposited on polycarbonate and polyimide substrate to confirm the possibility that polymer can be used as the substrate of nanoparticle arrays.

Conventional DC magnetron sputtering using Ar gas was used for the deposition (figure 3–1). Target materials were Cu, Au, Ag, Co, Ni, Si and Ti. The chamber was evacuated to less than 4×10^{-5} Pa, and operating pressure was 1.4 Pa (10 mTorr).

The deposited samples were post-treated by plasma of annealing in a stainless steel chamber (figure 3–2). Before the treatment, the chamber was evacuated to less than 4×10^{-5} Pa; the pressure increased to 2.7 Pa (20 mTorr) during the treatment. The samples were loaded using a load-lock system after the sample holder was heated to the desired temperature. The heat treatment of the sample was carried out in

an H₂ atmosphere at various temperatures, and the samples were cooled to room temperature in the load-lock chamber. Plasma treatment of the sample was conducted in an H₂ or Ar atmosphere without or with extra heating. A radio-frequency plasma of 13.56 MHz was generated by Au-coated three-turned Cu coil installed on a quartz plate that served as the lid of the chamber.

To enhance the energy transferred to the substrate from plasma, rf bias was applied at the substrate holder. Because the substrate was insulator, self-dc bias was induced by applying rf bias. In this case, the exposed part of substrate holder would be sputtered by the substrate self-dc bias if the holder was made with stainless steel, and it would result in the contamination of nanoparticle array sample. Therefore, the holder should be covered with hardly-sputtered materials such as tungsten and quartz. The schematic diagram of the substrate holder is shown in figure 3-3. The top part of substrate holder was covered with 1 mm tungsten plate, and a load-lock holder was made with quartz because tungsten was hard to be processed into complicated shape. The thickness of the load-lock holder was 1.8 mm. If it was thicker than 2 mm, self-dc bias would be consumed at the quartz load-lock holder. The self-dc bias and peak to peak voltage were measured by oscilloscope.

Measurement of substrate and chamber environment temperature was conducted by shielded thermal couple. The substrate temperature cannot be measured accurately when the rf bias is applied at the substrate, because rf interferes signals at the thermal couple even if it was shielded. In this case, we used the thermal tape for measuring substrate temperature (figure 3-4).

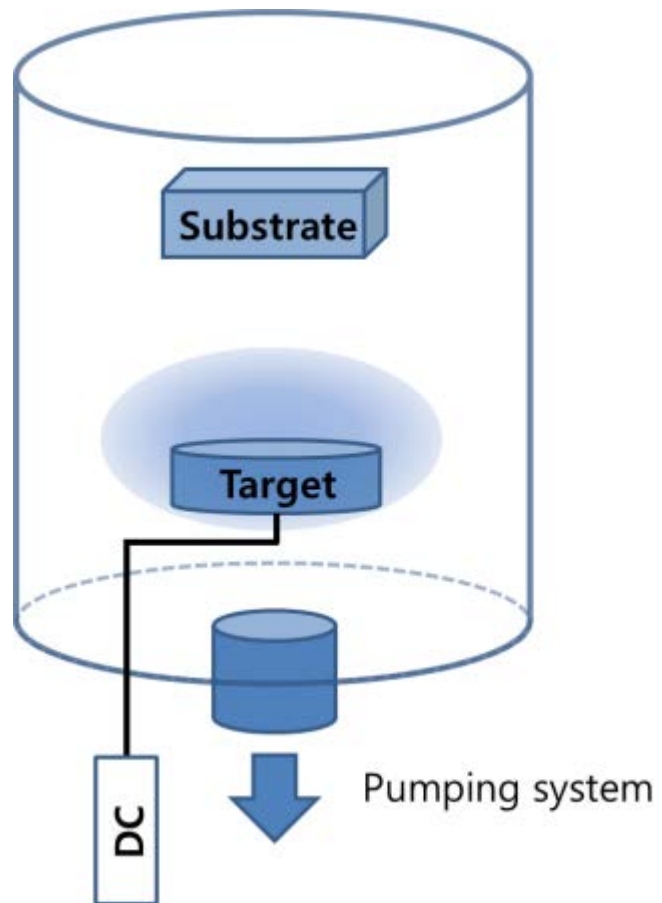


Figure 3–1. Schematic diagram of DC sputtering system

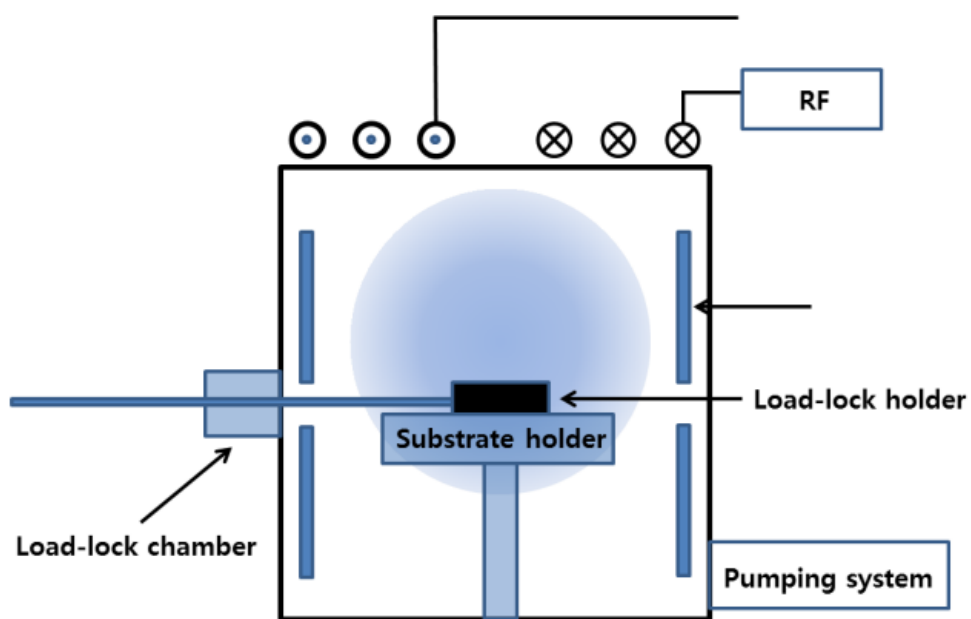


Figure 3-2. Schematic diagram of post-treatment chamber

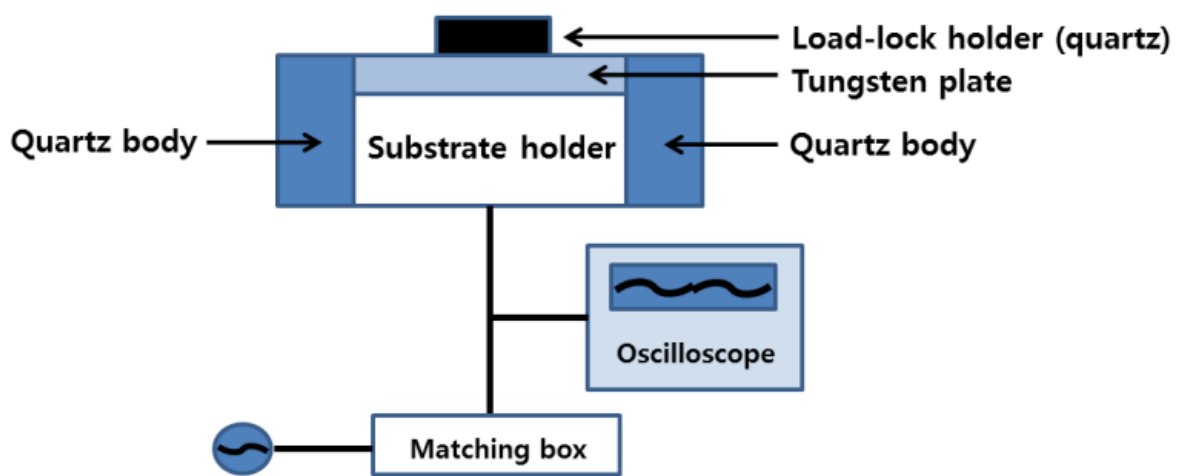


Figure 3-3. Schematic diagram of substrate bias part of post-treatment chamber



Figure 3-4. Image of the thermal tape which is attached on the substrate.

3.2 Analysis methods

1) Surface morphology analysis

Surface morphology and metal nanoparticle arrays geometry were analyzed by field-emission scanning electron microscopy (FE-SEM) (JEOL JSM6330F, HITACHI SU-70) operating at 5 kV and atomic force microscope (AFM) (NANOSTATION II). To analyze the periodicity of nanoparticle arrays, Fourier transform of AFM data was conducted.

2) Microstructure analysis

The microstructure was characterized by transmission electron microscopy (TEM) (Tecnai F20). The hole nucleation mechanism and the thickness of as-deposited film was revealed through TEM. Cross-sectional TEM samples were prepared using argon ion beam milling.

3) Film composition analysis

Concentration depth profiles were obtained by Auger electron spectroscopy (AES) (Perkin-Elmer, model 670).

4) Plasma parameter analysis

To analysis of plasma condition during the process, a single Langmuir probe (SLP) was used. The SLP is consist of metal probe tip, power and current measurement device. The single Langmuir probe tip was made with tungsten. The length of tip is 3 mm. Therefore, plasma did not affected by the tip because it was too small. The electric current value is varied with the applied voltage (I-V characteristic curve) as

shown in figure 3–5. When probe voltage increases over the V_p (region A), only electron get into the probe tip. If the applied voltage decreases below the V_p (region B), the electron which has larger energy than $e(V_p - V_b)$ is possible to get into the tip, whereas the low energy electron is reflected. Therefore, if the electron energy distribution is decided by Boltzmann factor, the I–V characteristic curve at region B can be expressed as exponential function. The probe current becomes 0 at the specific voltage. The voltage is called V_f (floating potential). With decreasing V_b lower than floating potential (region C), the electron current is reduced while ion current increases. As similar as region A, the current value is not changed significantly even if applied voltage is reduced. This current value is called ion saturation current.

Besides the SLP, we used WISE probe to measure the plasma parameter on real–times basis. It was useful for observing the plasma parameter effects on the producing nanoparticle arrays.

For minimizing plasma parameter difference between the substrate and the measuring tip part, the smaller plasma post–treatment chamber (mini–chamber) than the figure 3–2 chamber which was used in the other experiments was used during the plasma parameter analysis experiment (chapter 4.2 and 4.3.2) which was conducted with SLP and WISE probe. However, even if the size of the mini–chamber was smaller, it had the exactly same structure with the figure 3–2.

5) Optical property analysis

The absorption spectroscopy in the ultraviolet–visible spectral region was conducted to analyze the localized surface plasmon resonance of Cu nanoparticles.

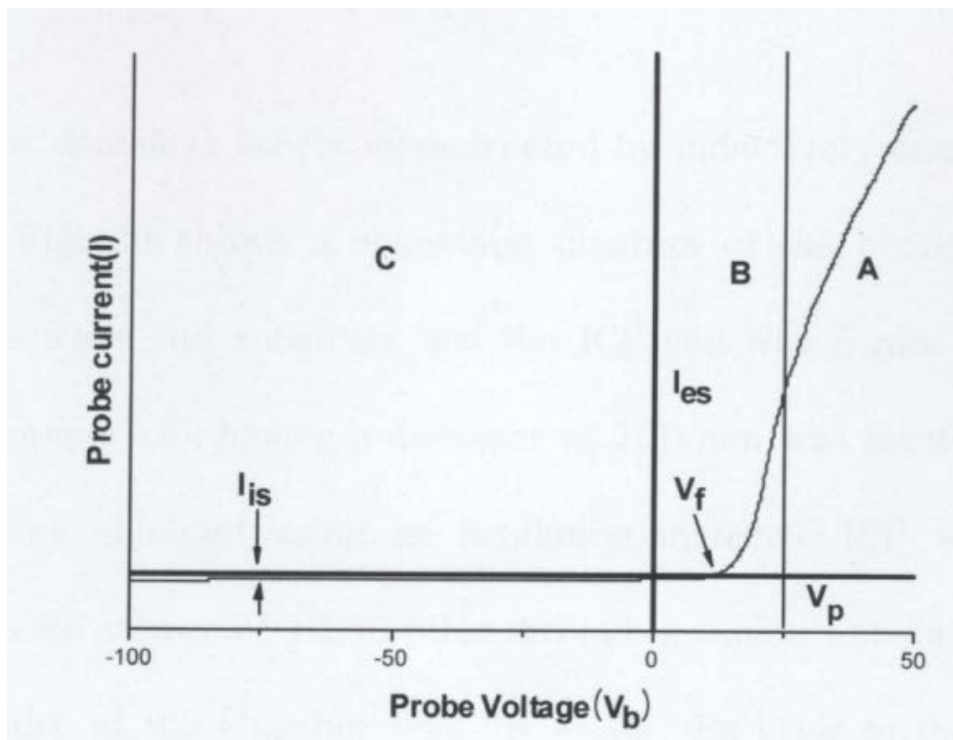


Figure 3-5. I-V characteristic for a single Langmuir probe. A : electron saturation region, B: electron retardation region and C: ion saturation region.

4. Results and Discussions

4.1 Formation of Cu nanoparticle arrays by plasma-induced dewetting

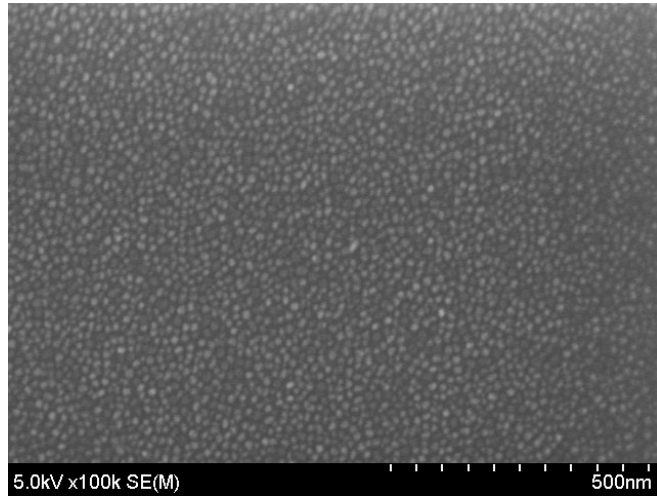
The initial experiment of producing metal nanoparticle array using plasma-induced dewetting was conducted with Cu thin film. Given that Cu is easy to dewet and sensitive to oxidation, Cu is a good material to analyze the effect of oxidation which occurs during the synthesizing process. The merit of plasma-induced dewetting in terms of oxidation will be revealed after comparing the process with thermal annealing (section 4.3).

Figure 4-2 shows the absorbance spectroscopy of the Cu nanoparticle arrays. 2 nm, 4 nm, 6 nm and 8 nm lines indicate spectroscopy data of the nanoparticle arrays shown in figure 4-1 (b), (c), (d) and (f), respectively. In nanoparticles, localized surface plasmon (LSP) is induced by electromagnetic wave, such as light, and it resonates with the light with a specific wavelength. This is called localized surface plasmon resonance (LSPR). When a 'pol,' which exists at the center between LSP, becomes a 'multi-pol' , the wavelength and amplitude of the peak at which LSPR occurs change. Because the number of pols increases with increasing particle size, changes in intensity and location of the absorbance peak are observed. (figure 4-2). Therefore, the plasma-induced dewetting process is suitable for plasmonics applications.

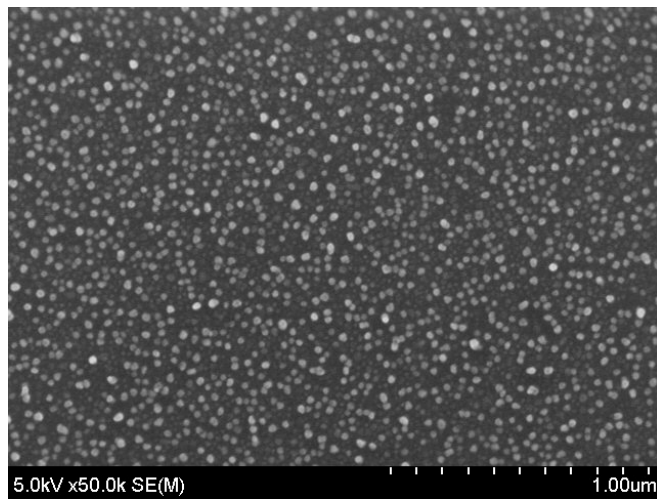
During the Ar plasma-induced dewetting process (figure 4-1), the measured process temperature was < 450 K, which is lower than the

usual thermal annealing temperature (> 573 K). Therefore, polymeric materials could be used as substrates as shown in figure 4-3 and 4-4. By varying the time and ICP power, Cu nanoparticle distribution was successfully controlled. The process temperatures were 450 K at 500 W ICP power and 413 K at 300 W ICP power. Because there are only a few precedents on controlling uniformity of nanoparticle arrays on the polymer substrate, the plasma-induced dewetting process would be a promising way for various applications.

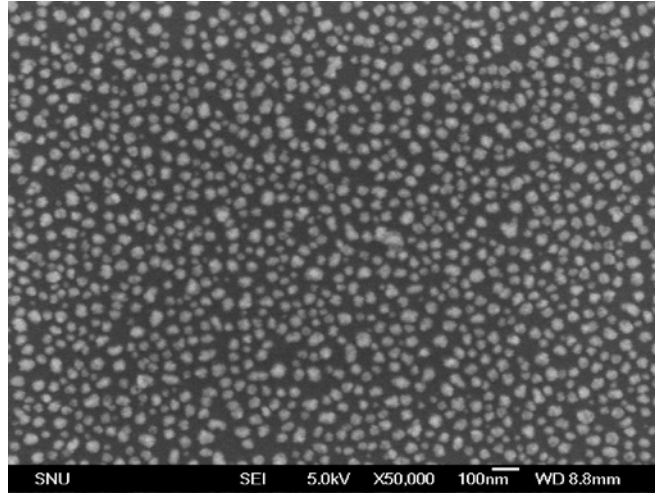
The reason that dewetting occurred at the low temperature is due to ion bombardment on the substrate surface. During the plasma treatment, ions bombard at the substrate surface with energy proportional to the sheath potential (scores of eV); the details on plasma energy will be discussed in section 4.3. Because ions hit the surface with energy equal to tens of thousands of degrees, the surface atom becomes mobile (figure 4-5). However, the ion energy is cannot be transferred beneath a few layers of the surface atoms. Therefore, the total system temperature can be maintained low, and the substrate damage can be minimized during the dewetting.



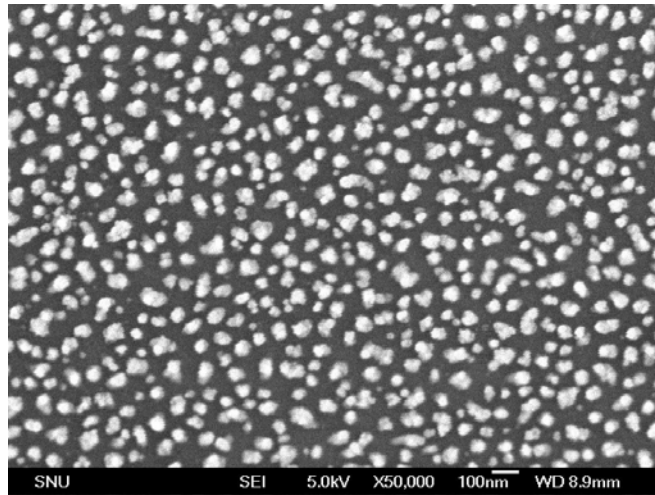
(a)



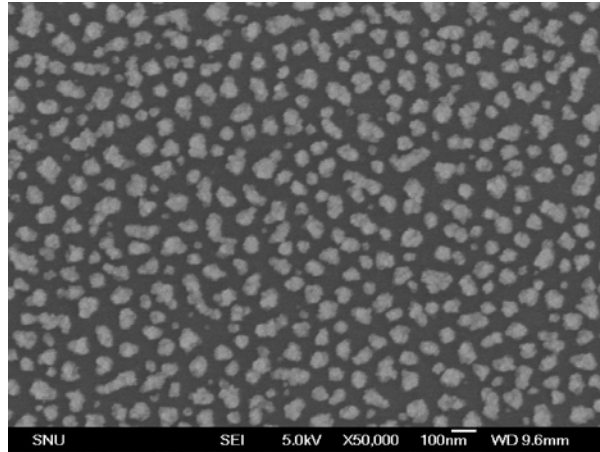
(b)



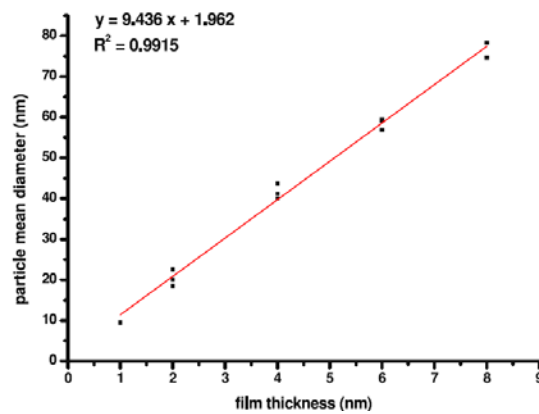
(c)



(d)



(e)



(f)

Figure 4–1 Cu nanoparticles after 500 W Ar plasma treatment for 1 h at 20 mT. The operating temperature was 450 K. The thicknesses of the Cu films were (a) 1 nm, (b) 2 nm, (c) 4 nm, (d) 6 nm and (e) 8 nm. Notice that (a) has a different scale bar. (f) Dependence of the average diameter of Cu nanoparticles as a function of theas–deposited Cu film thickness.

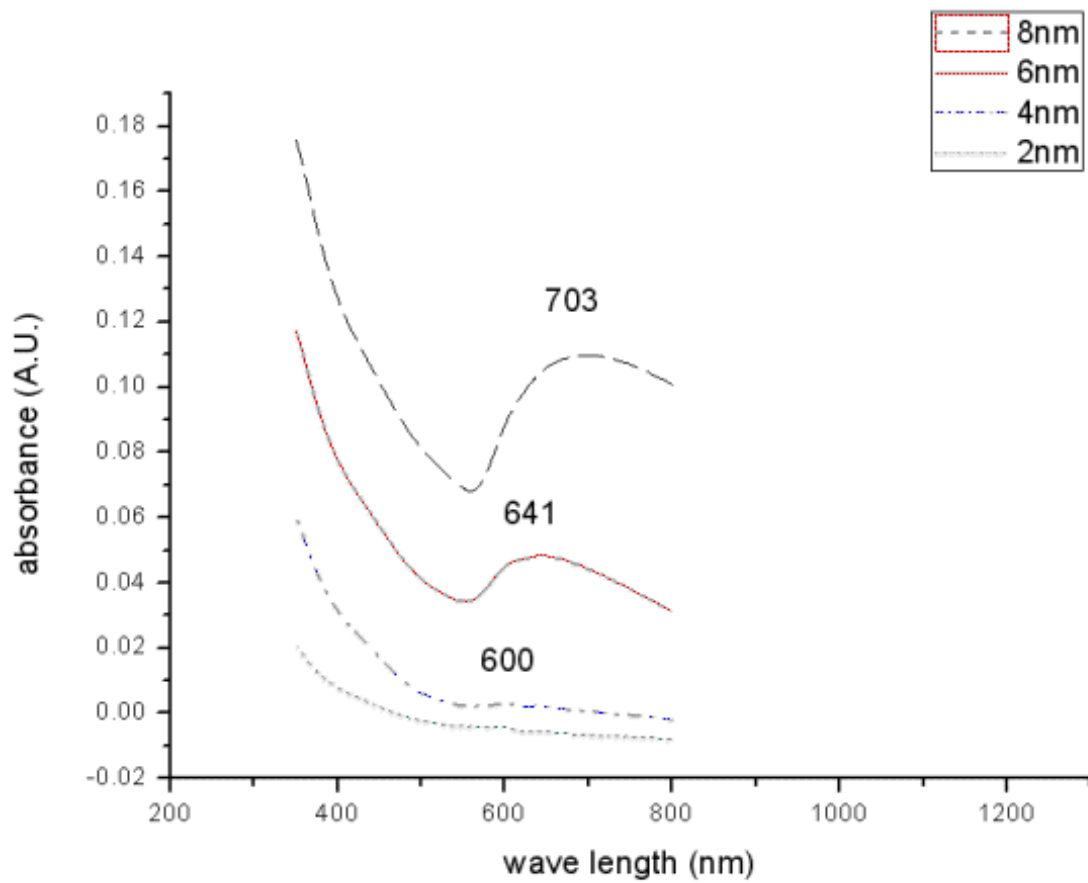
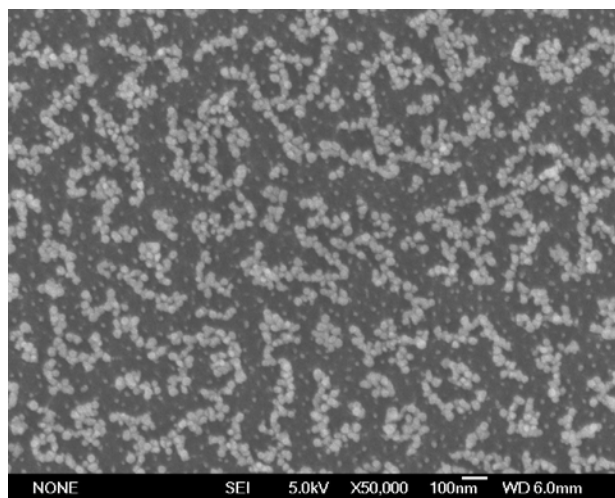
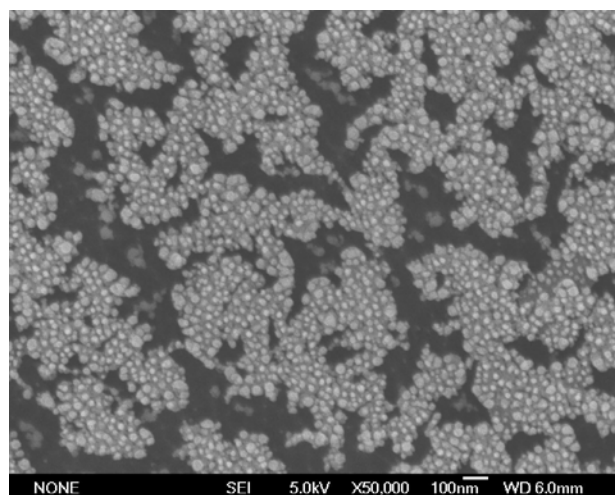


Figure 4-2. UV-vis spectroscopy measurement data of the various Cu nanoparticle arrays.

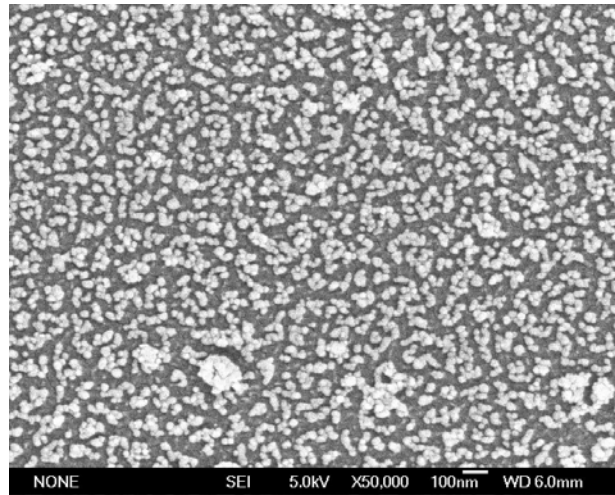


(a)

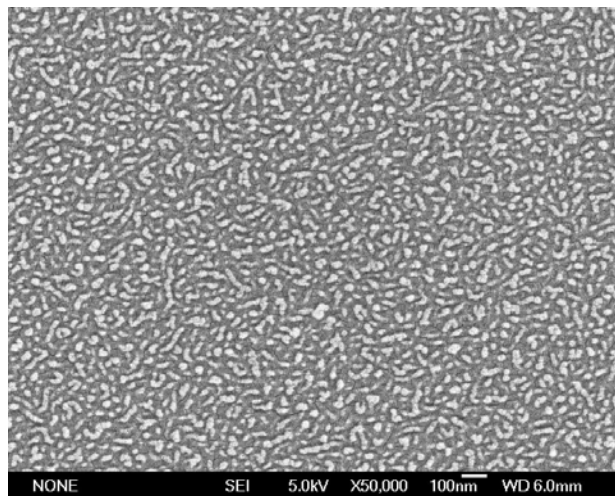


(b)

Figure 4–3. SEM images of Cu nanoparticles on polyimide (PI) substrate after (a) 300 W and (b) 500 W Ar plasma treatment for 10 min at 20 mT.



(a)



(b)

Figure 4-4. SEM images of Cu nanoparticles on polyimide (PI) substrate after 300 W Ar plasma treatment for (a) 10 min and (b) 30 min at 20 mT.

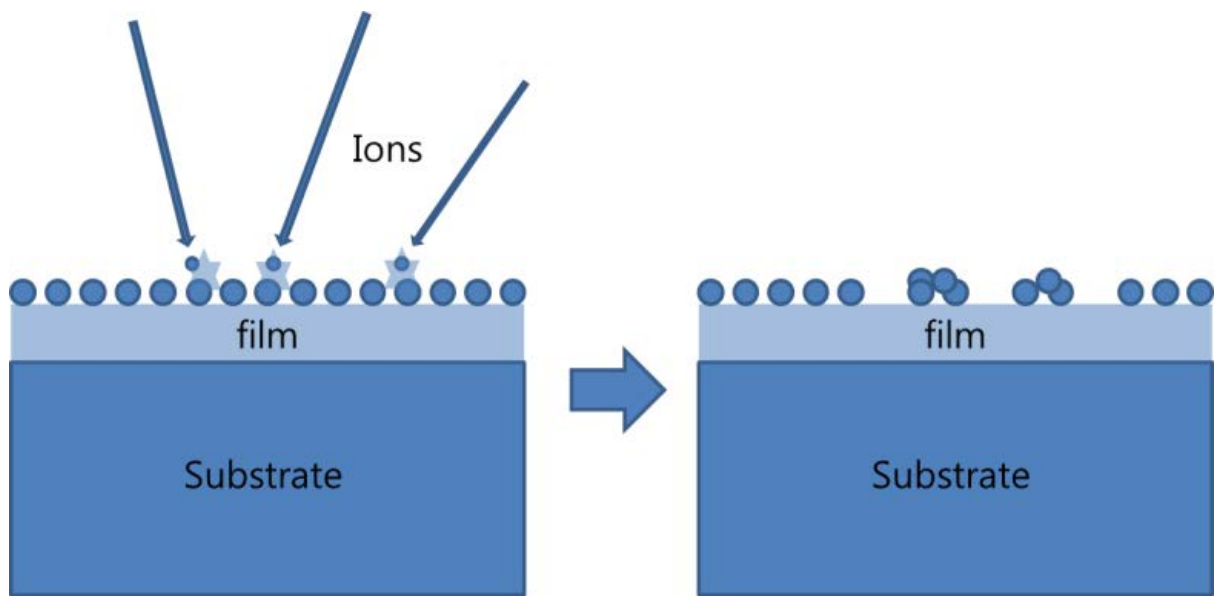


Figure 4–5. Schematic diagram of ion bombardment on substrate surface. Only the film surface atoms become mobile.

4.2 The hole nucleation mechanism of the plasma-induced dewetting

4.2.1 Surface morphology analysis with SEM

As mentioned experimental section, the stress-induced dewetting mechanism can be excluded from the possible mechanism of plasma-induced dewetting.

The morphology of the Cu nanoparticles after plasma treatment is similar to that of nanoparticles obtained by spinodal dewetting. However, the plasma dewetting of the Cu thin film did not proceed by this mechanism for the following reasons.

(1) The plasma treatment was carried out at temperatures far below the Cu melting temperature of 1358 K; therefore, the Cu dewetting proceeded in the solid-state. Additionally, although the melting temperature of Cu thin films can be lowered to 943 K [53], it is still much higher than our process temperature.

(2) The scaled results of the periodicity of the undulations with the film thickness conflict with the spinodal dewetting mechanism; in our process, $r \sim h$, whereas $r \sim h^{1.54 \pm 0.08}$ for spinodal dewetting; r and h refer to the average diameter of the particle and film thickness, respectively [54].

The sequence of Cu nanoparticle formation is shown in figure 4-6. In the first stage, holes began to form throughout the substrate. These holes expanded and coalesced with each other to form partially connected structures (i.e. a percolating structure) (figure 4-6 (d)). The partial connections of the remaining film material detached over time and,

eventually, the dewetting process terminates when elongated islands break up into spherical-shaped ones owing to Rayleigh instability [55, 56]. The whole process time is only 10 minute.

The key mechanism of the dewetting process is hole nucleation mechanism. Therefore, to determine the mechanism, the surface morphologies with respect to the process time in the early stage of the Cu film dewetting process were monitored with high magnification as shown in figure 4-7. Figure 4-7 (b) shows that holes had already started to form by surface perturbation after 20 s. The spacing between the holes can be evaluated from figure 4-7 (c), and it was found to be ~ 5 nm. The nucleated holes expanded while forming bicontinuous structures (figure 4-7 (c)-(e)). In this experiment, the Cu film transformed into uniformly distributed nanoparticles with an average diameter of 45 nm (figure 4-7 (f)).

4.2.2 TEM analysis

The high-resolution TEM (HR-TEM) images in figure 4-8 show that the grain size of the as-deposited Cu film is ~ 5 nm. The grain boundaries of the as-deposited Cu film can be seen in figure 4-8 (b). The TEM and SEM images in figure 4-7 and 4-8 show that the hole nucleation and growth proceeded along the grain boundaries, indicating that the plasma-induced dewetting progresses via a heterogeneous hole nucleation mechanism although the SEM morphology change closely resembles spinodal dewetting. Cross-sectional TEM images of as-deposited samples treated with Ar-plasma for 40 s are shown in figure 4-9. The deposited film was continuous with a thickness of ~ 5 nm (dark area in figure 4-9 (a)). After 40 s of Ar plasma treatment (figure 4-9

(b)), a hole was formed. The hole size (8 nm) was almost the same as that of the holes shown in figure 4–8 (d). TEM diffraction image of the 5 nm Cu film was shown in figure 4–10. Ring image means that the as-deposited film is polycrystalline film. D1, D2, D3 and D4 values are 2.494, 2.093, 1.501 and 1.279, respectively. The values mean that the film consisted of Cu and Cu oxide (CuO, Cu₂O, Cu₄O₃).

4.2.3. AFM analysis

In applications, geometry of nanoparticle is very important. For example, the ratio of nanoparticle's height and width defines the plasmonic properties. It also affects to property and morphology of nanowires when nanoparticle array is used as catalyst of nanowires. Therefore, atomic force microscopy (AFM) analysis was conducted. The AFM images of the Cu nanoparticles in figure 4–7 (f) are shown in figure 4–11. Figure 4–11 (b) shows that the height of the nanoparticles is <10 nm, indicating that the particles have a disc shape and not a spherical shape.

To show evidence for short-range order (SRO), we conducted a two-dimensional Fourier transform with the figure 4–11 AFM data which is particularly useful to identify any repeating patterns on the sample [57]. As shown in figure 4–12, the bright circle visible in the spectrum is proof of the SRO. The 4 bright points which is placed out of circle and the bright noise line are caused by vibration of the AFM device.

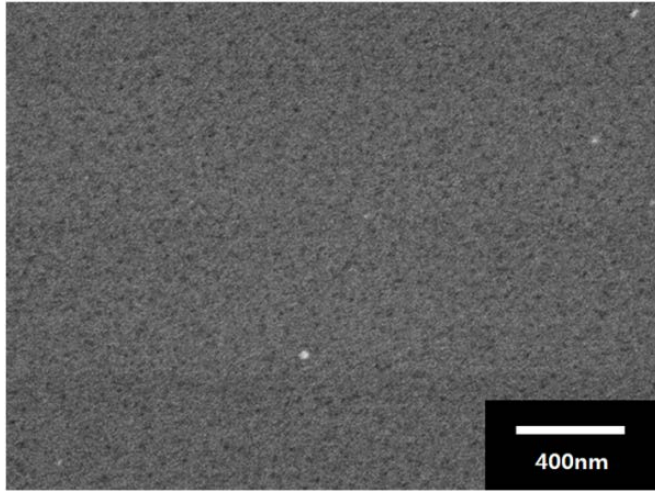
4.2.4 SLP analysis

Using plasma, sometimes sputtering or etching of substrate material is occurred during the treatment. To figure out whether

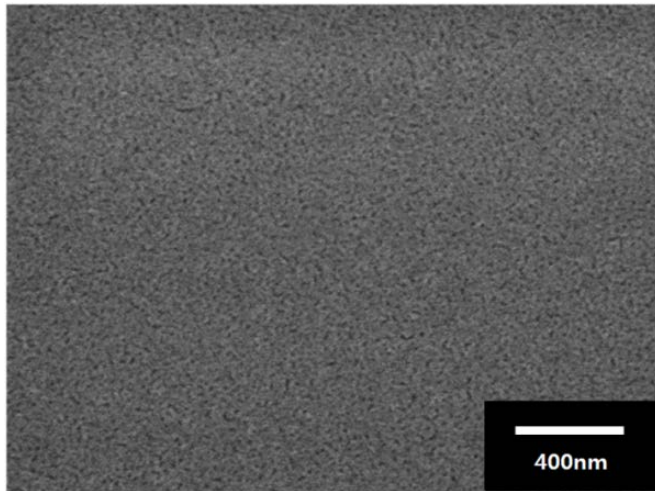
sputtering of Cu is occurred during dewetting process or not, plasma analysis was conducted by WISE probe. The plasma parameter data were double checked by SLP. In figure 4-6 and 4-7 conditions, the electron temperature (T_e) was measured to be 3.1 eV. The ions hit the Cu film surface with energy that is equivalent to the sheath potential; the sheath potential is related to the T_e as follows:

$$\Phi_{sh} = \Phi_p - \Phi_f = \frac{Te}{2} + Te \ln \sqrt{M/2\pi m} \quad (\text{eq. 4.1})$$

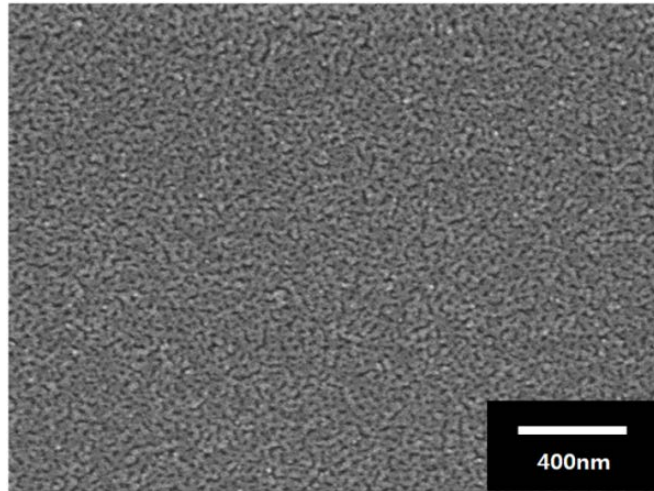
where Φ_{sh} , Φ_p , Φ_f , M , and m are the sheath potential, plasma potential, floating potential, ion mass, and electron mass, respectively [58]. Therefore, the energy of Ar ($M = 40$ amu) ions which bombard the substrate can be expressed as $5.2 T_e$, and bombardment energy of a single ion was calculated to be 16.1 eV because T_e was 3.1 eV. The calculated energy indicates that sputtering of Cu and Au atoms did not occur during plasma treatment. The sputtering yield is calculated to be almost 0 [59].



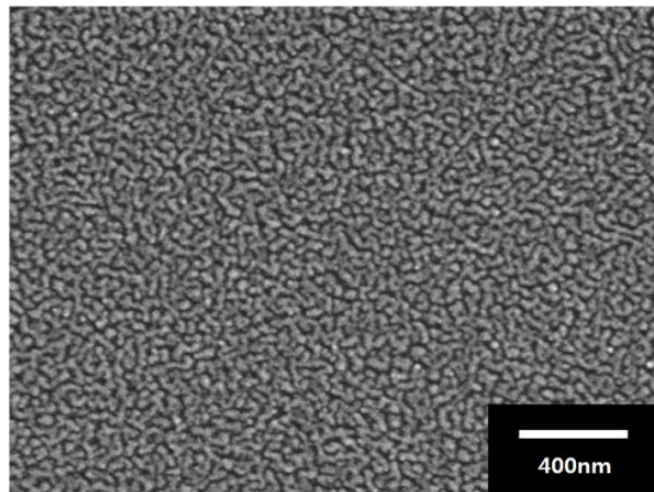
(a)



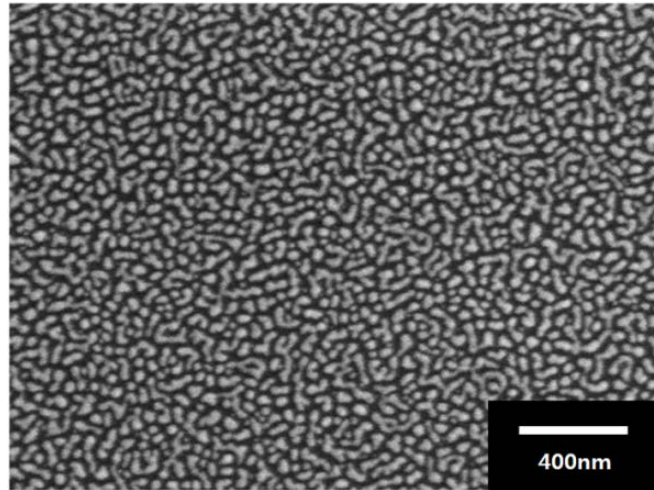
(b)



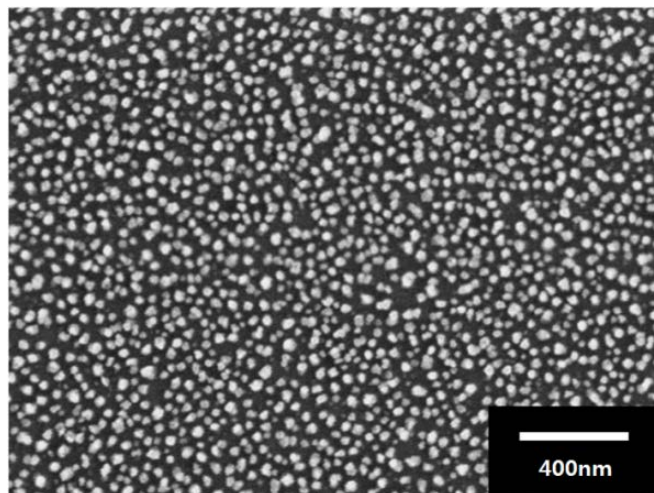
(c)



(d)

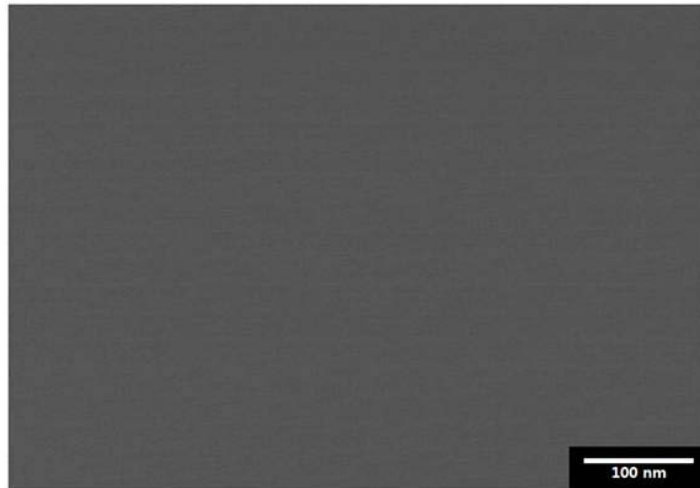


(e)

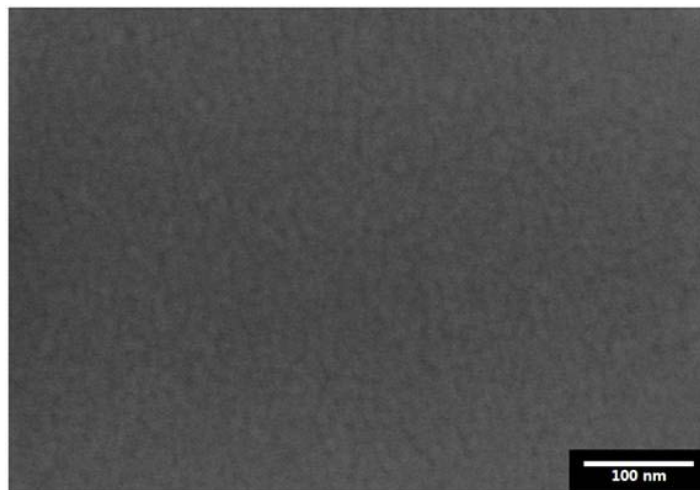


(f)

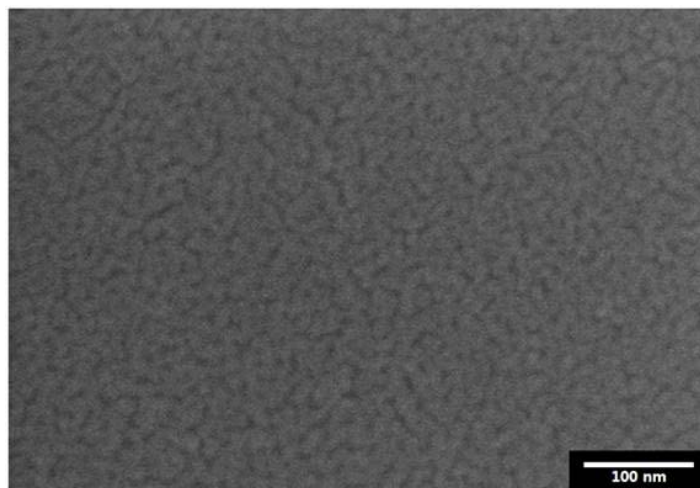
Figure 4-6. SEM images of 5 nm Cu films after 750 W Ar plasma treatment at 20 mT for different times: (a) as-deposited film, (b) 1 min, (c) 1.5 min, (d) 2 min, (e) 2.5 min and (f) 10 min.



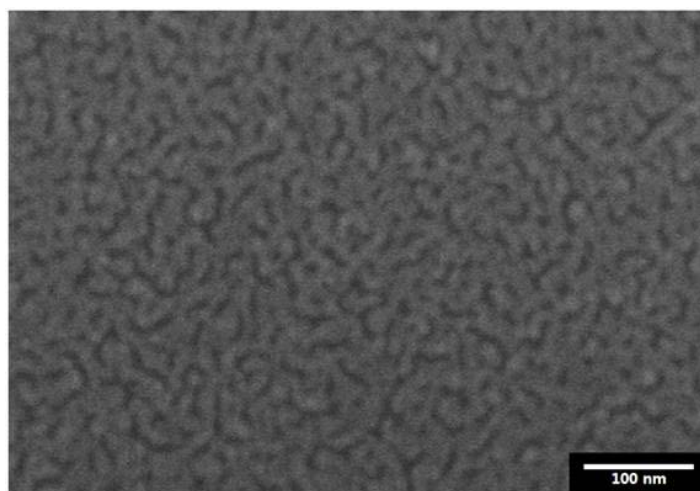
(a)



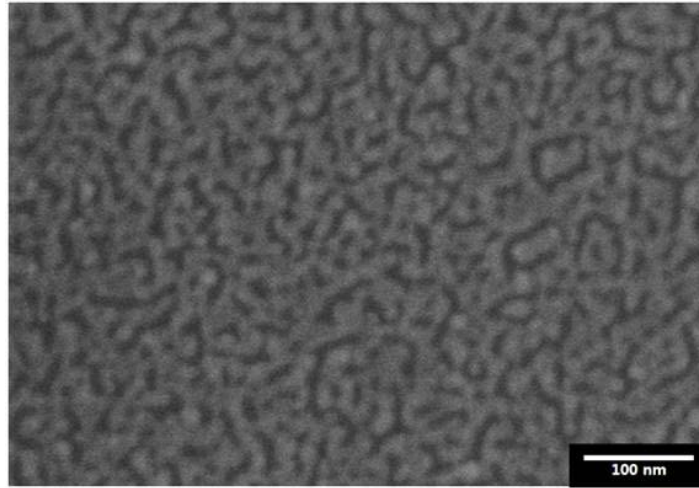
(b)



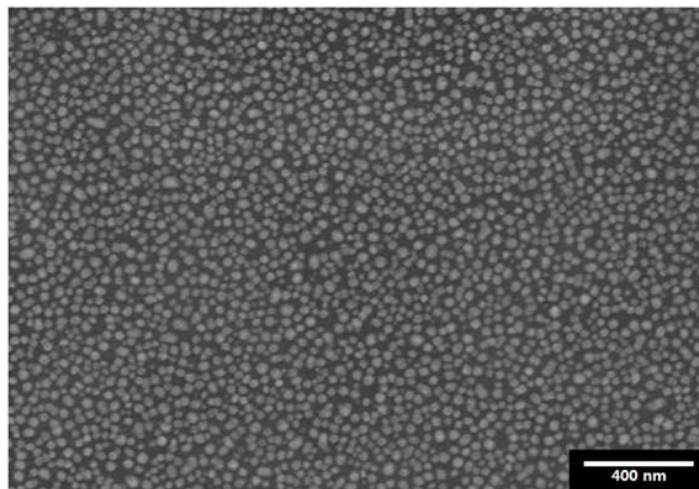
(c)



(d)

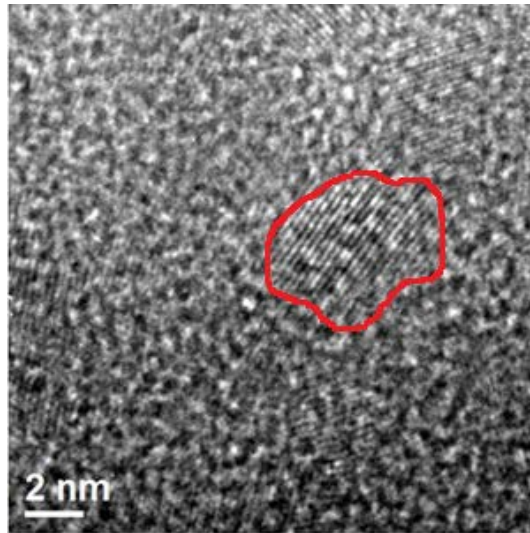


(e)

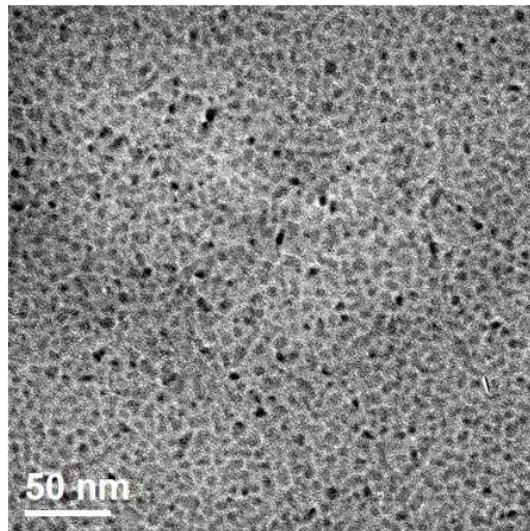


(f)

Figure 4-7. FE-SEM images of 5 nm Cu films after 750 W Ar plasma treatment at 20 mT for different times: (a) as-deposited film, (b) 20 s, (c) 30 s, (d) 40 s, (e) 50 s, and (f) 10 min. Note that (f) has a different scale bar.

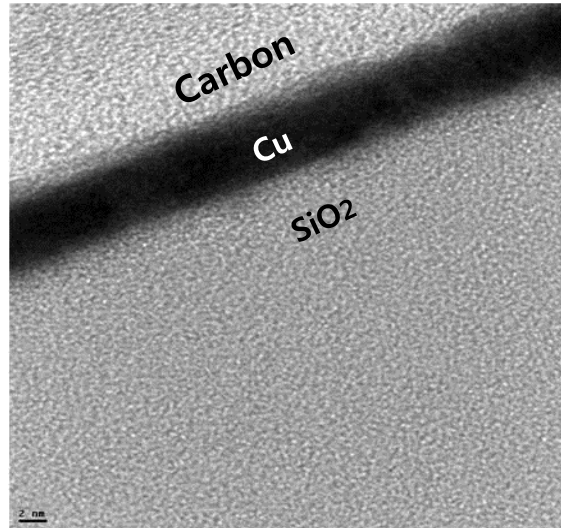


(a)

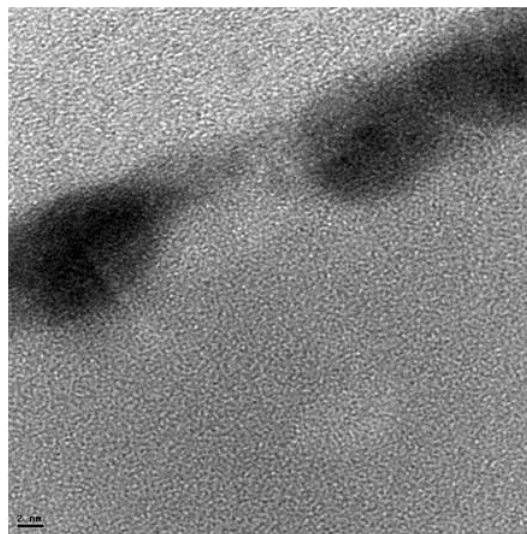


(b)

Figure 4–8. HR–TEM images of as–deposited 5 nm Cu film. Note that (a) and (b) have different scale bars.



(a)



(b)

Figure 4-9. Cross-sectional TEM images of Cu films: (a) as-deposited film and (b) after Ar plasma treatment for 40 s. (figure 4-7 (d) sample)

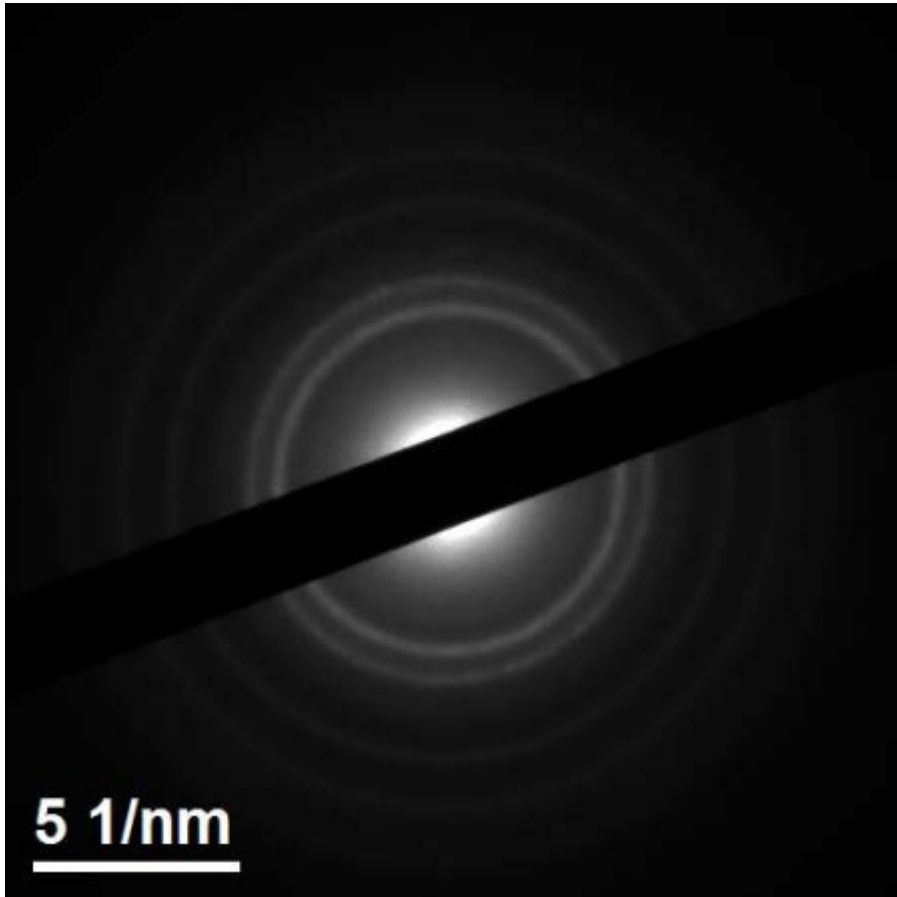
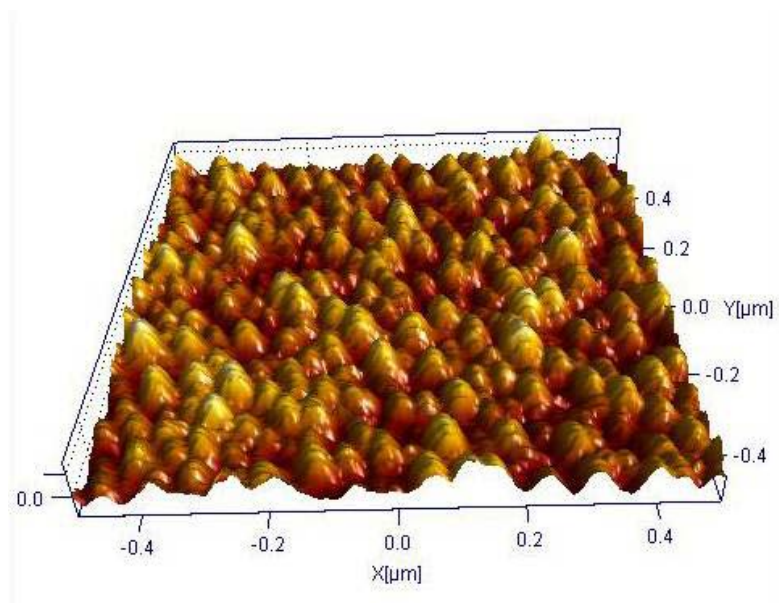
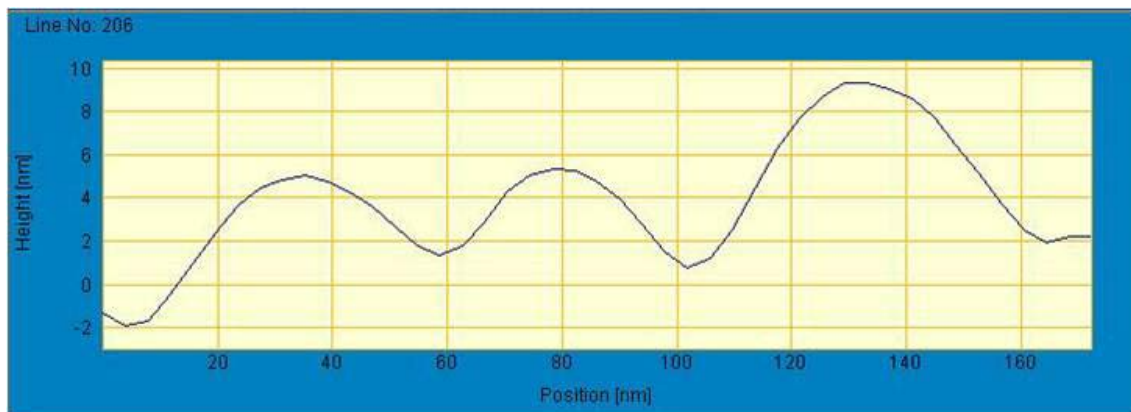


Figure 4–10. Diffraction image of 5 nm Cu thin film.



(a)



(b)

Figure 4-11. AFM image of the Cu film: (a) the surface image and (b) the height curve in the cross-sectional direction.

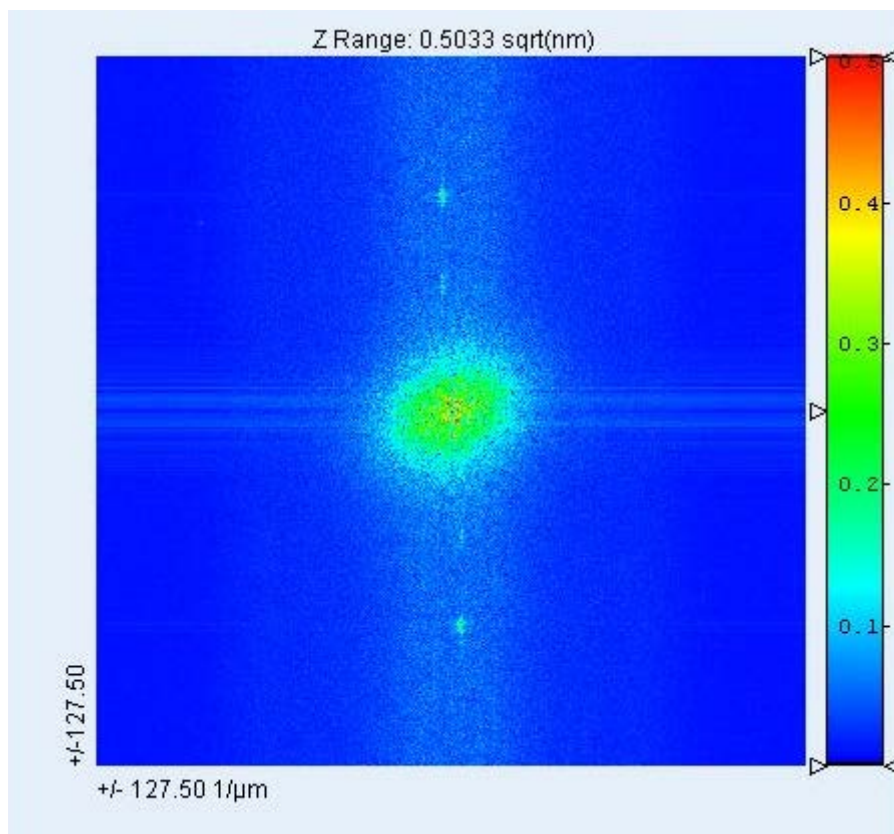


Figure 4-12. Image of a two-dimensional Fourier transform data

4.3 Uniformity control of nanoparticle array

4.3.1 Process temperature effect

To compare the uniformity of nanoparticles which is produced by plasma-induced dewetting and thermally activated dewetting, thermal annealing was conducted at various temperatures. It is generally known that Cu agglomeration during thermal annealing or plasma treatment at high temperatures is interrupted by Cu oxidation, and H_2 is required to suppress the oxidation and enhance agglomeration [60, 61]. Therefore, H_2 was used during the thermal annealing process.

According to Gadkari et. al [48], a few nm Cu films are possible to dewet at > 373 K. Therefore, we conducted the thermal annealing at 473, 573 and 773 K for 2 hours (figure 4-13). The sample treated for 2 hours at 473 K was barely dewetted (figure 4-13 (a)). Hence dewetting rate is very slow at 473 K, thermal annealing at 473 K seems to be inappropriate for actual nanoparticle producing process. Cu nanoparticles formed at 573 K seemed uniform (figure 4-13 (b)-1). However, as shown in figure 4-13 (b)-2, small nanoparticles were distributed randomly and residues of the film were observed in the high magnification image. At 773 K, as shown in figure 4-13 (c), the film dewetted completely, but the uniformity of nanoparticles was inferior to that of plasma dewetted particles (figure 4-1 (c)). Consequently, nanoparticles dewetted by thermal annealing shows worse size uniformity than that by plasma treatment. There are two reasons for this phenomenon.

1) Coarsening effect and oxidation

Ar and H₂ plasma treatments were conducted with and without extra annealing. In this chapter, oxidation effect is also explained even if it is not directly related with the uniformity of nanoparticle arrays because it is inevitable when thin films are annealed and oxidation is always important for applications. Figure 4-14 and 4-15 show the results of Ar and H₂ plasma treatment of 4 and 8 nm Cu films without extra heating. The measured substrate temperature was < 450 K. Figure 4-16 shows the dewetting results of Ar or H₂ plasma treatment 4 nm film at 773 K. At low temperature (< 450 K), it was evident that completely dewetted Cu nanoparticles were produced by the Ar plasma from 8 nm film (figure 4-14 (b)), while the dewetting process was still underway when H₂ plasma was used (figure 4-15 (b)). This indicates that the rate of dewetting was much higher in the Ar plasma treatment. The results shown in figures 4-14 and 15 are not in accordance with previous reports which states that H₂ radicals enhance the migration of Cu because of the oxidation [36, 22-24].

However, when 4 nm Cu films were H₂ and Ar plasma treated at 773 K, the Cu film dewetted much more clearly in the H₂ plasma (figure 4-16 (a)); the film treated with H₂ plasma (figure 4- 16 (a)) was completely dewetted without residues, while that treated by Ar plasma (figure 4-16 (b)) was not. This indicates that H₂ radicals play an important role at high temperatures during plasma dewetting due to the high oxidation rate. The threshold partial pressure of Cu oxidation was calculated to confirm whether Cu oxidation occurs at 450 and 773 K. The values were 9.85×10^{-32} atm and 1.09×10^{-15} atm at 450 K and 773 K, respectively, and they were lower than the partial pressure of O₂ in

the process chamber, which was 2.7×10^{-11} atm. Accordingly, Cu film oxidizes under both temperature conditions. However, from a kinetics perspective, the surface oxidation of Cu films dramatically increases at high temperature. Therefore, at 450 K, the oxidation rate is lower than that at 773 K. Thus, the H₂ effect is not as evident at 450 K as it would be at higher temperatures. Ion bombardment which transfers high energy to the surface atoms (section 4.1, figure 4-5) is the reason that plasma-induced dewetting proceeded rapidly even if the process temperature was low.

The operating temperature is an important factor in obtaining uniformly distributed particles via plasma dewetting. At 773 K, the nanoparticles formed by H₂ plasma dewetting on 4 nm Cu films (figure 4-16 (a)) had a particle morphology similar to those synthesized from a heat treatment (figure 4-13 (c)) and had a less uniform particle distribution than those synthesized via H₂ plasma-induced dewetting at < 450 K (figure 4-15 (a)). At higher temperatures, Ostwald ripening and migration and the coalescence of islands are accelerated in metal thin films, which cause an increase in the standard particle size deviation [63-65]. Because plasma dewetting was conducted at low temperature, uniformly sized nanoparticles can be produced.

The anti-oxidation effect of plasma-induced dewetting was confirmed by AES depth profile. In figures 4-17 and 4-18, the AES and SEM data of the two samples which was treated by thermal annealing at 573 K and 500 W Ar plasma are shown. The annealing was conducted at 573 K because the appropriate temperature which could induce the dewetting of Cu nanoparticle with minimum oxidation is 573 K according to figure 4-13. The sample annealed at 773 K would be oxidized too

much because of the high temperature. Thus, 773 K treated sample is unworthy of comparing with a sample by plasma treatment. Silicon was used as the substrate for the two samples because silicon oxide substrate is inappropriate for analyzing oxidation ratio in the film.

Below 1 nm depth from the surface, oxygen ratio was measured to be about 50 % in both samples. Below 1 nm, percentage of the oxygen is always higher than Cu, while oxygen content is abruptly reduced and Cu content increases. Si content increases and Cu content decreases with depth because the substrate is Si. The fact that Si substrate is revealed much more on the plasma treated surface (figure 4-18 (b)) than the annealed surface should be noticed (figure 4-18 (a)). Because the AES analysis proceeds vertically downward from the surface, the Si concentration shown in AES data is detected from the start of the measurement; data of the plasma treated sample shows much more Si contents than annealed one at the surface. Moreover, the surface of the Si substrate was badly oxidized because it was exposed in air for a long time. Therefore, the surface oxygen concentration (< 1 nm) shown in AES data (figure 4-17 (b)) is measured higher than the actual oxygen concentration on the surface. There are two reasons that the surface oxygen ratio is detected to be high on the surface: 1) the effect of revealed Si substrate, 2) ion bombardment on the surface atom which cannot transfer the energy to the atoms below the surface.

As shown in AFM data (figure 4-11), average nanoparticle thickness is about 10 nm. According to the data, the thickness of large nanoparticles is about 15 nm. Given that Cu and oxygen contents are 5 % at 13 nm and 0 % at 15 nm in figure 4-17 (b), Cu did not diffuse into the Si substrate. On the other hand, in thermal annealing (figure 4-17 (a)),

Cu and oxygen contents are measured to be 10 % until the nanoparticles are as large as 20 nm. The thickness of the thermally annealed sample would be about 5 nm which is the same thickness as the as-deposited film because the dewetting did not much proceed (figure 4-18 (a)). Therefore, Cu was diffused into the substrate by annealing, and it resulted in contamination of the nanoparticles and substrate. The contamination by diffusion process is widely known, and it has become a serious problem [66]. The problem does not occur in plasma-induced dewetting because the process is conducted at low temperature. Moreover, oxidation of nanoparticles which is the most serious problem in producing Cu nanoparticles also can be prevented. If oxidation barrier layer, such as BTAH [7], is deposited after plasma-induced dewetting process, it could be a promising technique for producing anti-oxidized Cu nanoparticle arrays.

2) hole nucleation morphology

To understand the uniformity difference between nanoparticles produced by thermal annealing and plasma-induced dewetting, the hole nucleation process was monitored and compared at same temperatures. Figures 4-19 (a) and (b) show Cu films after thermal annealing at 653 K in an H₂ environment and plasma treatment in Ar, respectively; the temperature was elevated to 653 K during plasma treatment by plasma heating (no extra heating). The processing time was 1 min for both samples. The reason for conducting the plasma treatment with 750 W ICP power, figures 4-6 and 4-7 plasma condition, and running the thermal process at 653 K was that 450 K was not high enough to deliver sufficient thermal energy to dewet the Cu thin film without plasma; the

chamber temperature normally increases to 450 K when using 500 W plasma. Although holes were nucleated heterogeneously in both processes, their morphologies were quite different after the same treatment time. The number of holes nucleated in the plasma-treated sample was approximately 10 times greater than that in the thermally annealed sample. Moreover, the plasma-treated sample had much smaller hole sizes than the thermally annealed sample. According to Gadkari et. al [48], holes are not nucleated in all grain boundaries, so the holes are sparse and separated by distances greater than the grain size. The figure 4-19 (a) is consistent with this explanation on the conventional hole nucleation. On the other hand, in plasma-induced dewetting, holes are nucleated in all grain boundaries and their distance is exactly the same as the grain size. It means that a new hole nucleation phenomenon is observed in our experiment. Because a large number of small-sized holes were nucleated in the same area, dewetting took place more uniformly by the plasma process, resulting in more uniform particle sizes and space distributions.

4.3.2 Ion bombardment energy effect

To figure out the effect of plasma parameter to the nanoparticles, electron temperature (T_e) was controlled by varying pressure. Experiments are conducted with 4 nm Cu films. Figure 4-20 shows SEM images of the Cu nanoparticles after the dewetting processes at 20 and 100 mT. The plasma parameters used in the experiment shown in figure 4-20 are listed in Table 4-1. From the figure, it is observed that larger particles with worse size and space uniformity were formed at higher pressure.

Figures 4-21 and 4-22 show the dewetting process with respect to process time. At 20 mT, holes were nucleated at much more sites (figure 4-21 (a)); they grew with the so-called “percolating structure” (figure 4-21 (b)); and isolation of the film proceeded uniformly (figure 4-21 (c)). At 100 mT, significantly fewer holes were nucleated (figure 4-22 (a), (b)); moreover, they were not generated uniformly, resulting in non-uniform dewetting (figure 4-22 (c)). Therefore, nanoparticles were formed with much lower uniformity at 100 mT. The substrate temperatures were 653 and 626 K at 20 and 100 mT, respectively. In section 4.3.1, we found that non-uniform particles were formed at high temperatures. Because the temperature difference was less than 30 K and the substrate temperature was higher at 20 mT than at 100 mT, the temperature effect can be neglected in this experiment.

The change in dewetting morphologies with pressure is related to the change in the plasma parameter. As shown in Table 4-1, the plasma density (N_e) was the same at 20 mT and 100 mT, but the electron temperature (T_e) at 20 mT was higher than at 100 mT. T_e is determined by the particle balance in the global model. T_e decreased with an increase in the gas pressure because electrons lose energy through electron-neutron collisions, which are inelastic and momentum-transferring collisions [49].

The mean free paths of Ar atoms were calculated for different process pressures. They were 1.6 and 0.3 mm at 20 and 100 mT, respectively. These were much greater than the sheath lengths at the same pressures, which were calculated by Child’s Law [49] to be 0.069 and 0.055mm at 20 and 100 mT, respectively. In this case, a collisionless sheath is formed, and the sheath potential can be calculated using T_e

measured by the equation 4.1. The sheath potentials at 20 and 100 mT are determined to be 16.1 and 10.4 V, respectively, from the measured T_e values (Table 4-1).

After the sheath potential is obtained, the energy flux transferred to the substrate from the plasma can be calculated using the global model.

$$P_{abs} = e J_i A_{eff,s} \epsilon_{T,s} \quad (\text{eq. 4.2})$$

where P_{abs} , J_i , $A_{eff,s}$, and $\epsilon_{T,s}$ are the absorbed power at the substrate, ion flux density, effective area for particle loss at the substrate, and total energy loss at the substrate, respectively. The energy flux absorbed to the substrate by ion bombardment per unit area is P_{abs}/A_{eff} . The ion flux, J_i , was calculated by [20]

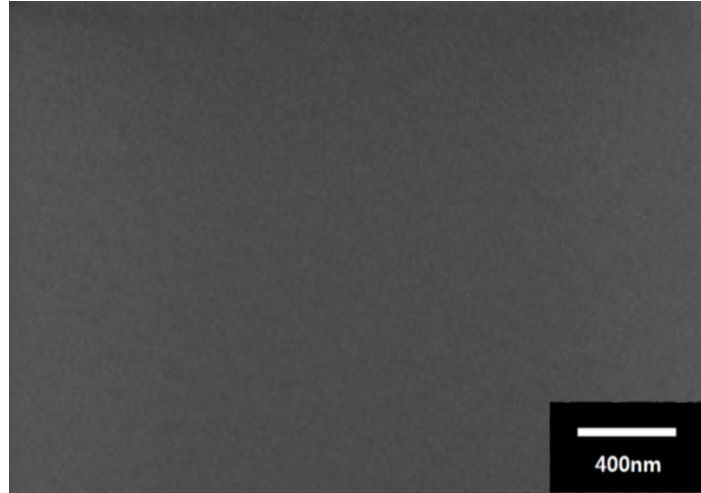
$$j_i = n_e \sqrt{kT_e/m_i} \exp(-0.5) \quad (\text{eq. 4.3})$$

The calculated energy fluxes are 0.12 and 0.06 J/cm²s at 20 and 100 mT, respectively. The total energy transferred to the substrate at 20 mT is two times larger than that at 100 mT. As a result, more holes are generated at 20 mT, causing the uniformity difference in figures 4-21 and 4-22.

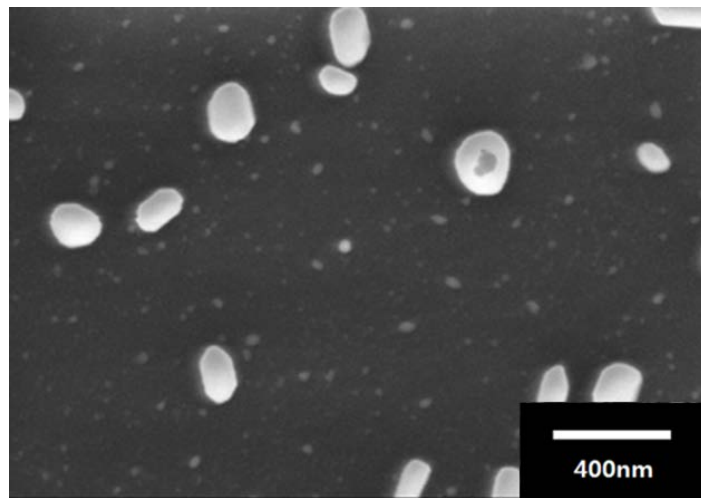
The effect of energy transfer was examined while controlling other process parameters. When the energy transfer was enhanced by substrate bias at the same pressure, the uniformity improved

significantly, as shown in figure 4-23. The sample was treated as the same as that in the experiment shown in figure 4-20 (b), except that the substrate bias was -50 V.

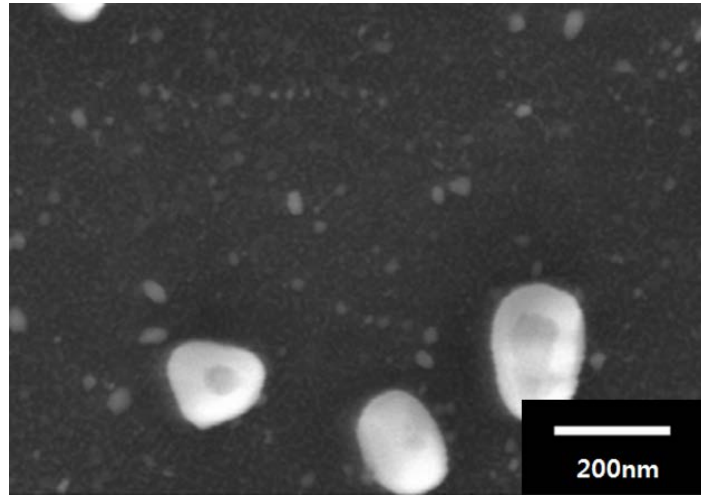
The energy transfer and the particle uniformity can also be increased by increasing the RF power (figure 4-24). The sample treated at 750 W shows higher uniformity compared to that treated at 400 W. As shown in Table 4-2, T_e and N_e are higher at 750 W than at 400 W, and therefore, the transferred energy is also higher at 750 W. Consequently, the uniformity of the Cu nanoparticle array can be enhanced by varying the plasma parameters to a particular process regime in which the amount of energy transfer per unit area and time is high.



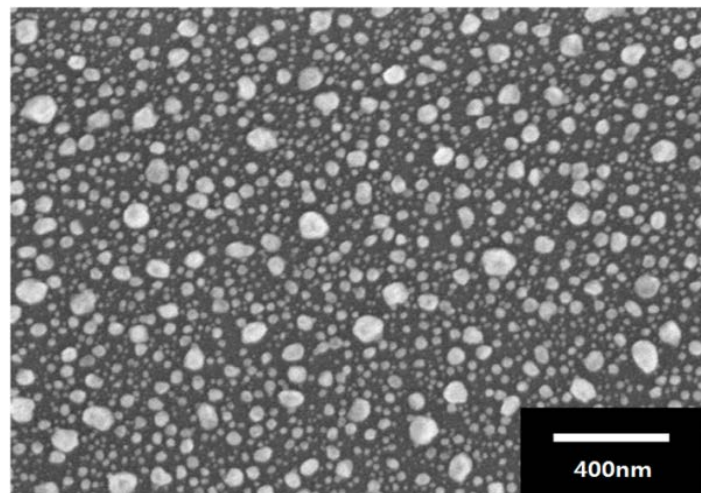
(a)



(b)-1

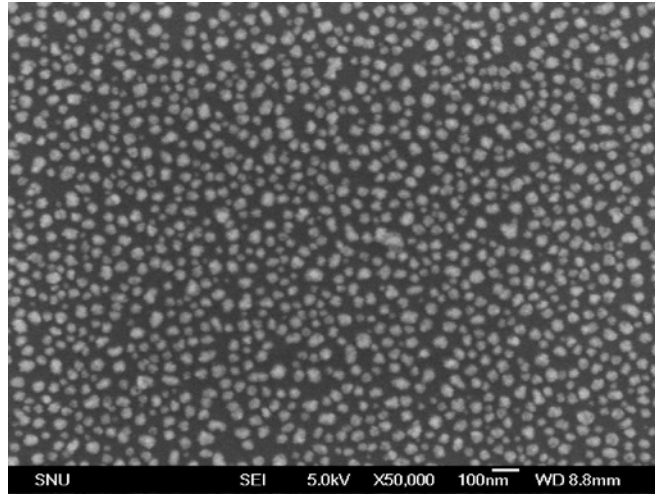


(b)-2

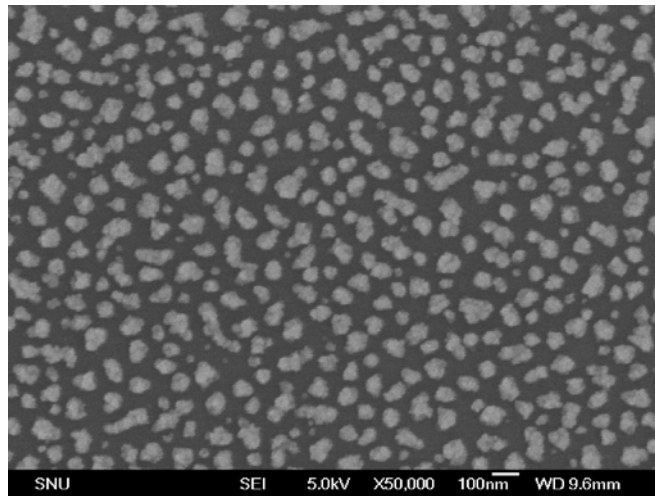


(c)

Figure 4-13. SEM images of the 4 nm Cu/SiO₂ samples after heat treatment with H₂ gas for 2 h at (a) 473, (b) 573 and (c) 773 K. Note that (b)-2 has a different scale bar. The images of (b)-1 and (b)-2 are for same sample.

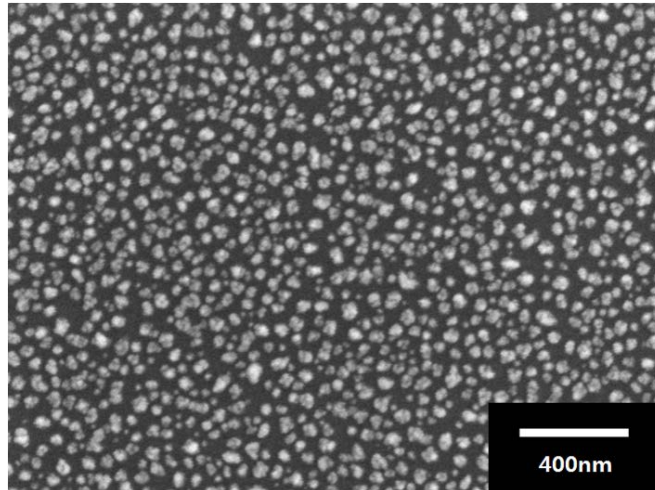


(a)

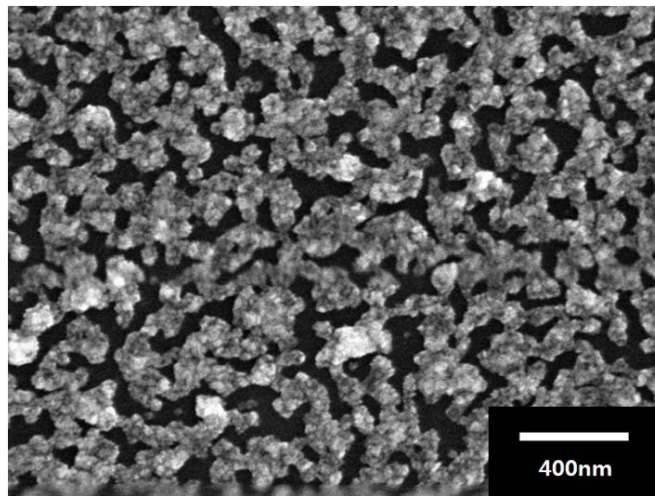


(b)

Figure 4-14. SEM images of the Cu/SiO₂ samples after the 500 W Ar plasma treatment for 1 h at 20 mT. The operating temperature was 450 K. The thickness of the Cu films was (a) 4 nm and (b) 8 nm. The same images were shown in figure 4-1.

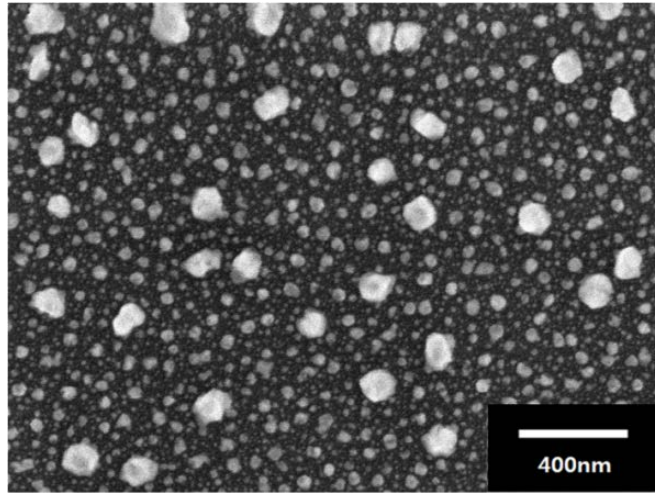


(a)

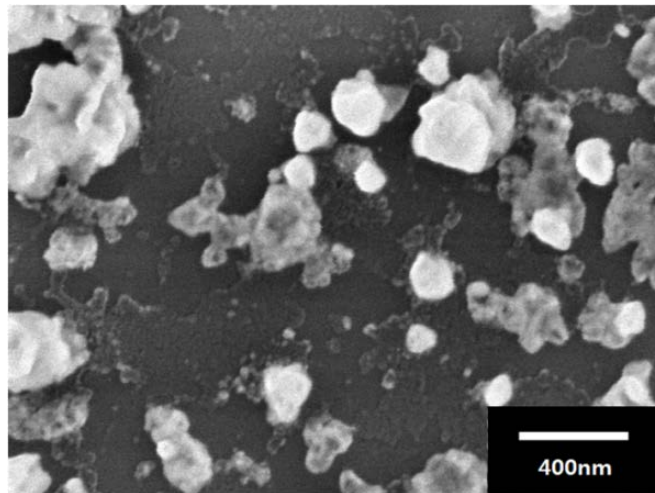


(b)

Figure 4–15. SEM images of the Cu/SiO₂ samples after the 500 W H₂ plasma treatment for 1 h at 20 mT. The operating temperature was 420 K. The thickness of the Cu films was (a) 4 nm and (b) 8 nm.

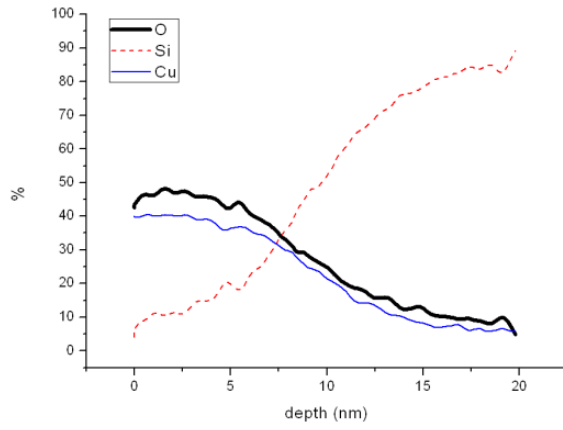


(a)

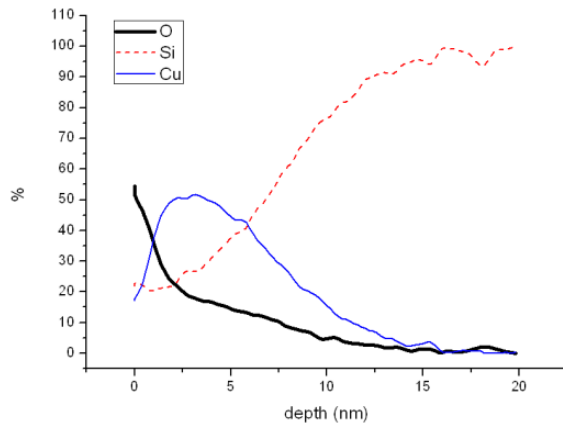


(b)

Figure 4–16. SEM images of the 4 nm Cu/SiO₂ samples after the 500 W plasma treatment in (a) H₂ and (b) Ar at 773 K for 1 h.

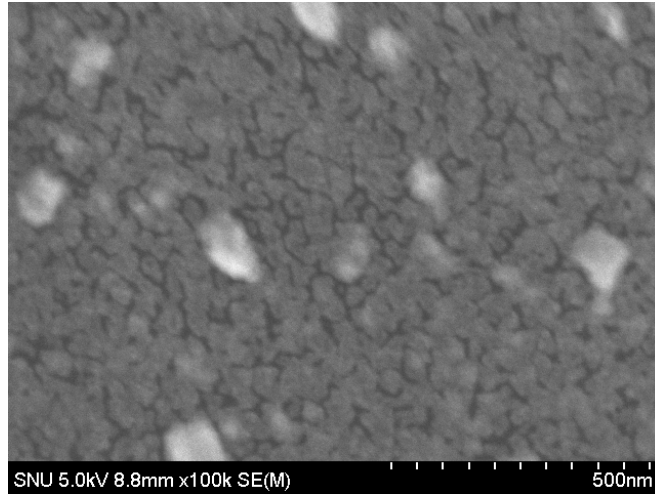


(a)

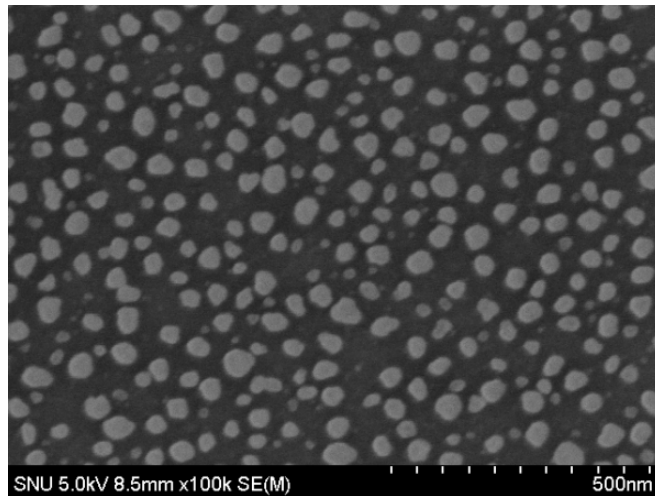


(b)

Figure 4-17. AES data of (a) thermally annealed 4 nm Cu film and (b) Ar plasma treated 4 nm Cu film on Si substrate.

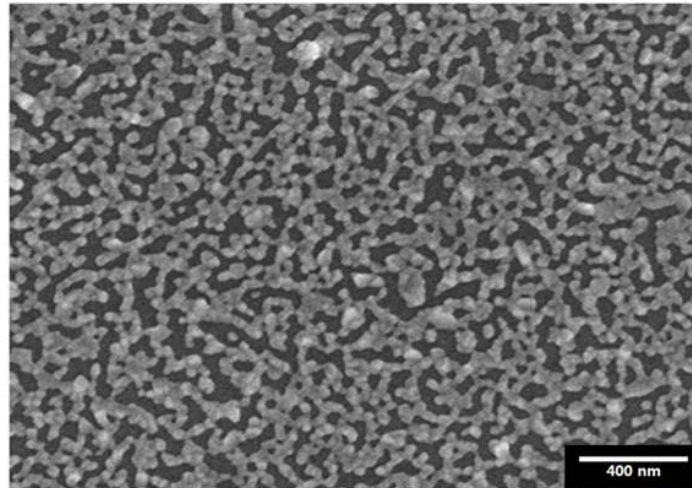


(a)

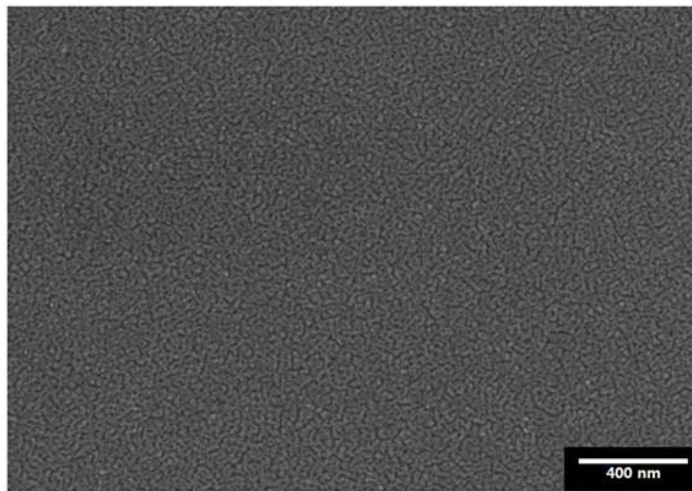


(b)

Figure 4–18. SEM images of the 4 nm Cu/Si samples after (a) the 573 K annealing and (b) the 500 W plasma treatment for 30 min.

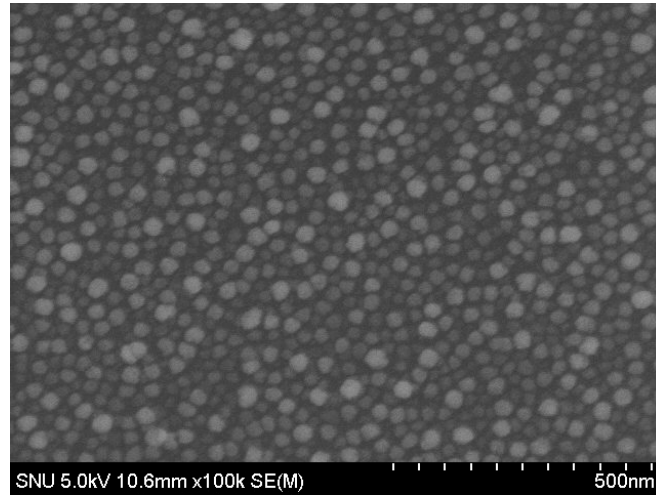


(a)

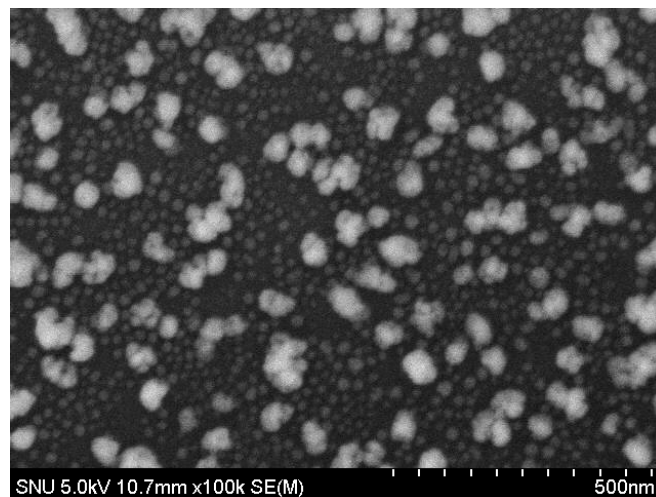


(b)

Figure 4–19. FE–SEM images of 5 nm Cu films (a) after heat treatment with H₂ gas for 1 min at 653 K and (b) after 750 W Ar plasma treatment for 1 min. The plasma treatment condition of (b) was the same as figures 6 and 7.



(a)

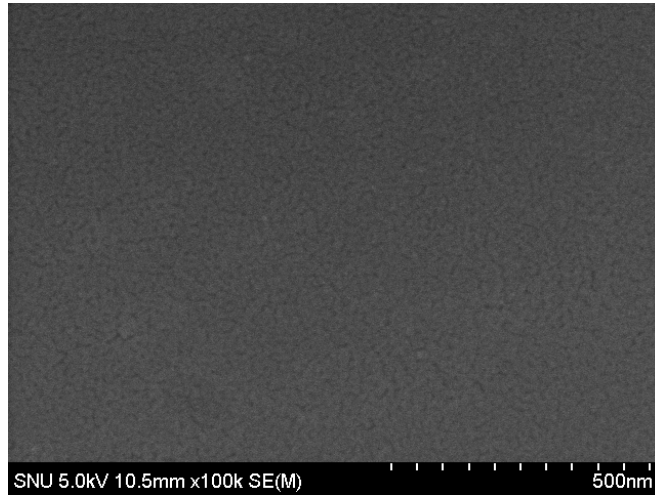


(b)

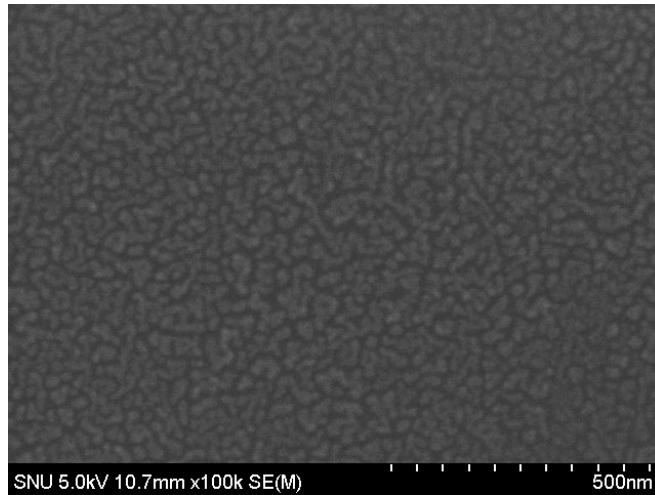
Figure 4–20. FE–SEM images of Cu nanoparticle arrays after Ar plasma treatment for 1 hour. The operating pressures were (a) 20 mTorr and (b) 100 mTorr.

| | Pressure (mTorr) | Plasma density (cm^{-3}) | Electron temperature (eV) |
|-----|---------------------|--|------------------------------|
| (a) | 20 | 2.7×10^{11} | 3.1 |
| (b) | 100 | 2.7×10^{11} | 2.0 |

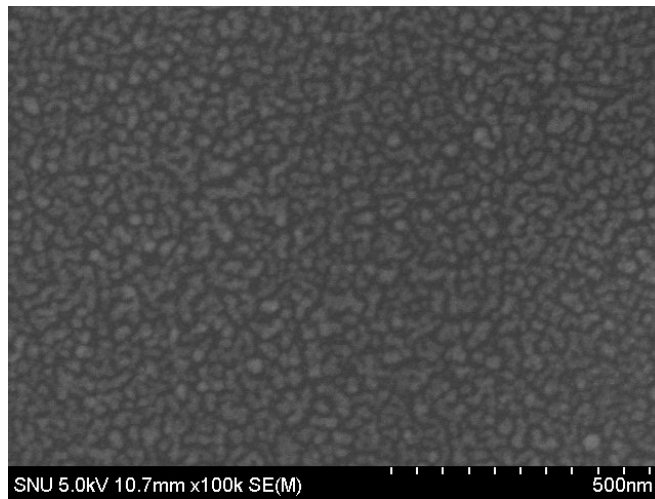
Table 4-1. Plasma parameter of figure 4-20 experimental condition



(a)

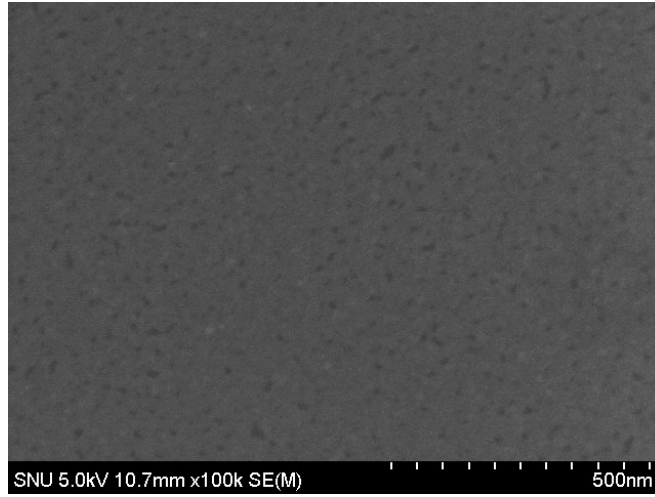


(b)

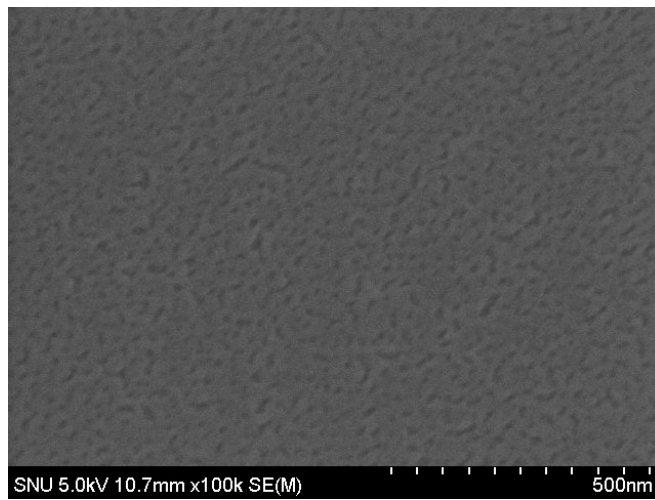


(c)

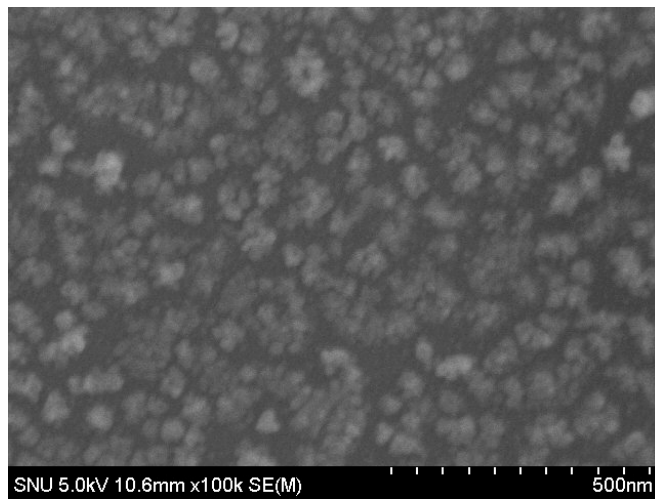
Figure 4-21. FE-SEM images of 4 nm Cu film after the Ar plasma treatment at 20 mTorr: (a) 30 S, (b) 1 min and (c) 2 min.



(a)



(b)



(c)

Figure 4-22. FE-SEM images of 4 nm Cu film after the Ar plasma treatment at 100 mT for: (a) 30 S, (b) 1 min and (c) 2 min.

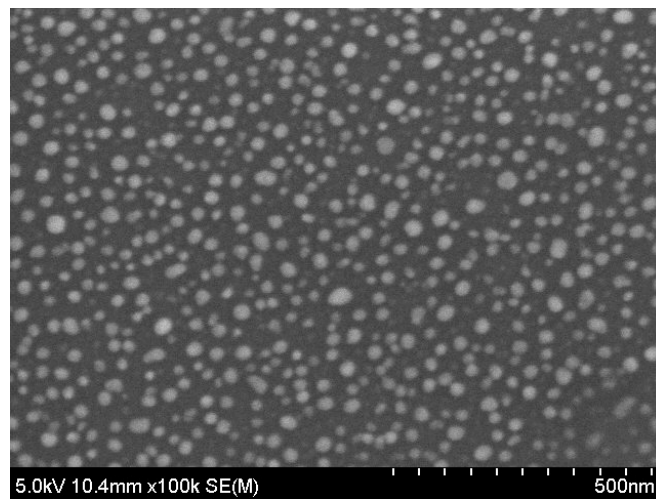
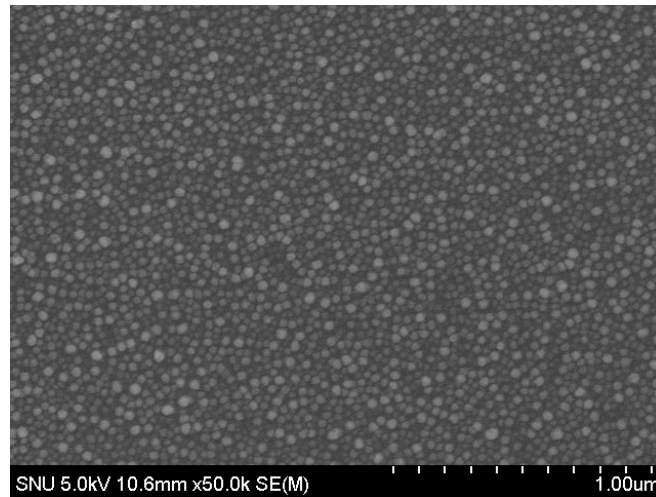
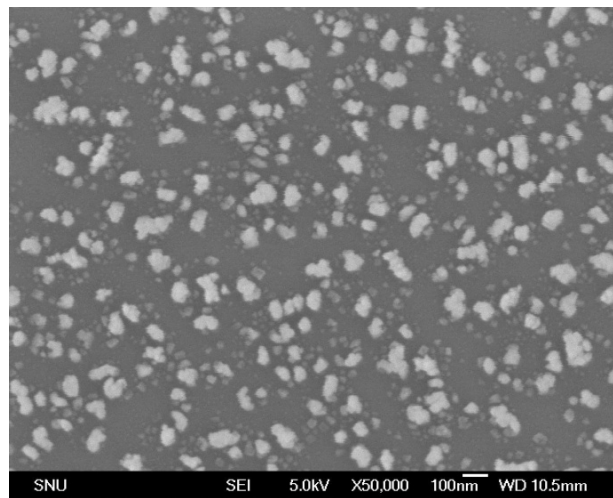


Figure 4–23. FE–SEM images of Cu nanoparticles array after 1 hour Ar plasma treatment at 100 mT and 190 W. Induced self–DC bias on the substrate was -50 V.



(a)



(b)

Figure 4–24. FE–SEM images of Cu nanoparticles array after 1 hour Ar plasma treatment. The operating pressures was 20 mTorr. Induced RF powers were (a) 750 W and (b) 400 W.

| | Pressure (mTorr) | RF power (W) | Plasma density (cm ⁻³) | Electron temperature (eV) |
|-----|---------------------|--------------------|--|---------------------------------|
| (a) | 20 | 750 | 2.7×10^{11} | 3.1 |
| (b) | 20 | 400 | 1.4×10^{11} | 2.5 |

Table 4-2. Plasma parameter of figure 4-20 experimental condition.

4.4 Various metal nanoparticle arrays produced by plasma-induced dewetting

4.4.1 Low melting temperature metals

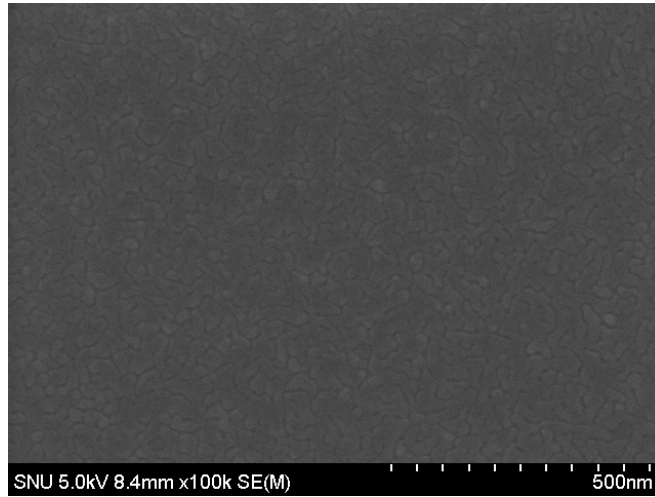
After producing Cu nanoparticle arrays, we tried to produce Au, Ag and Al nanoparticle arrays. Al nanoparticle array was failed to be synthesized (figure 4-25). Even if 12 hours Ar plasma treatment, dewetting did not proceed further (figure 4-25 (b)). Though agglomeration of the film observed after 12 hours H₂ plasma treatment, the dewetting rate was too slow to use the process for the mass production (figure 4-25 (c)). However, in Au and Ag 5 nm film, the nanoparticle arrays were successfully produced (figure 4-26). The particle size difference between Au and Ag nanoparticles was attributed to the surface energy difference. Unlike in the case of the Cu film, grain boundaries on the as-deposited Au film surface could be clearly observed by SEM (figure 4-27 (a)) because of the relatively high surface energy of Au [67]. As same as Cu, Au plasma-induced dewetting proceeds through heterogeneous hole nucleation; hole grows via grain boundaries (figure 4-27).

4.4.2 High melting temperature metals

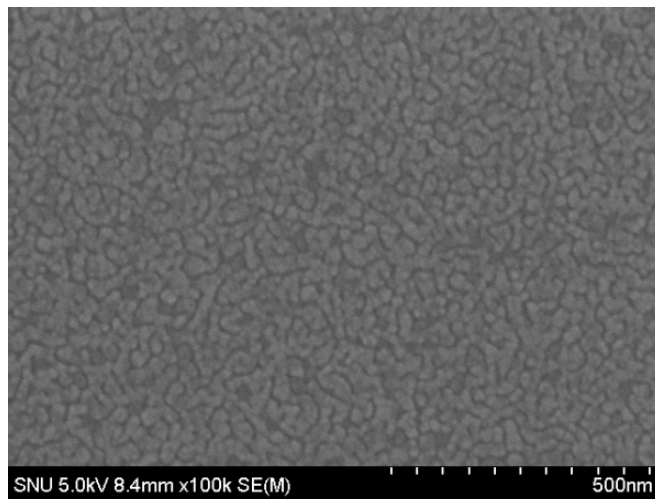
The melting point of Si, Ni, Co and Ti was too high to dewet the films using the previous experimental condition. Therefore, 30 V self dc bias (50 W rf bias) was applied to the substrate to enhance the ion bombardment energy. Using substrate bias, nanoparticle arrays were successfully produced (figure 4-28). Usually, Si nanoparticle arrays

which are used for the light absorption layer of the solar cell are annealed for 12 hours at 1173 K. However, in plasma-induced dewetting, the process time was less than 2 hours. Moreover, the substrate temperature was elevated to 520 K which is far lower than 1173 K.

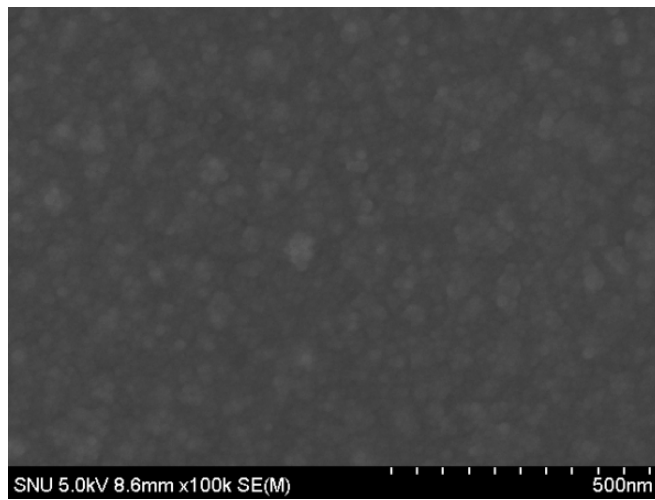
A SEM image of the middle stage of the Ti plasma-induced dewetting is shown in figure 4-29. The morphology was the same as Cu and Au plasma-induced dewetting. Consequently, hole nucleation and growth proceed via grain boundaries even if the melting point of the film is high.



(a)

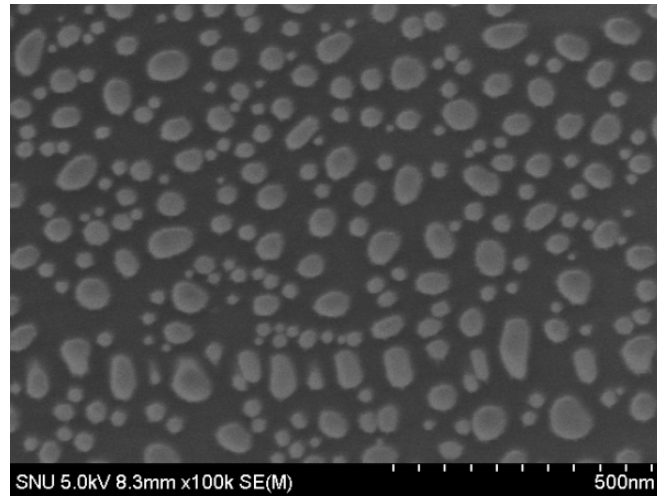


(b)

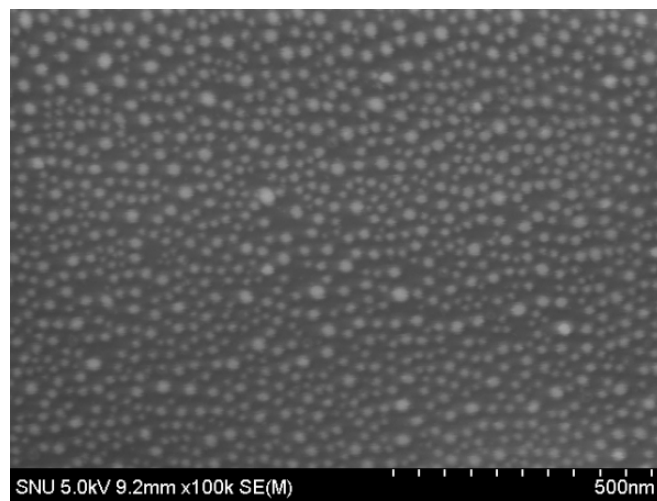


(c)

Figure 4-25. FE-SEM images of the 5 nm Al/SiO₂ samples; (a) as-deposited sample, (b) after 12 hours 700 W Ar plasma treatment, (c) after 12 hours 700 W H₂ plasma treatment.

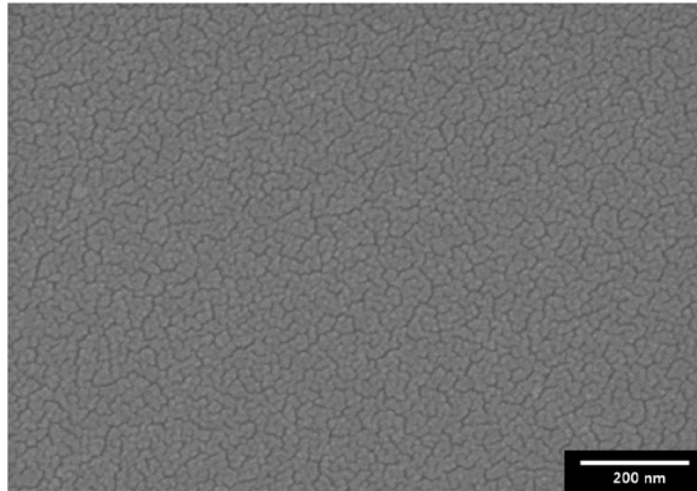


(a)

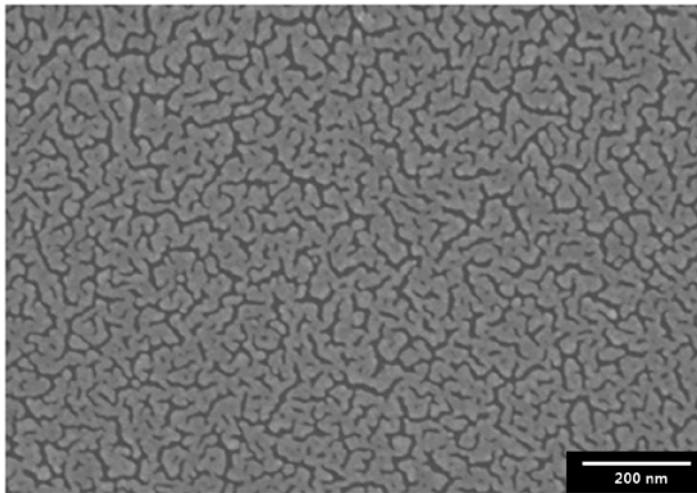


(b)

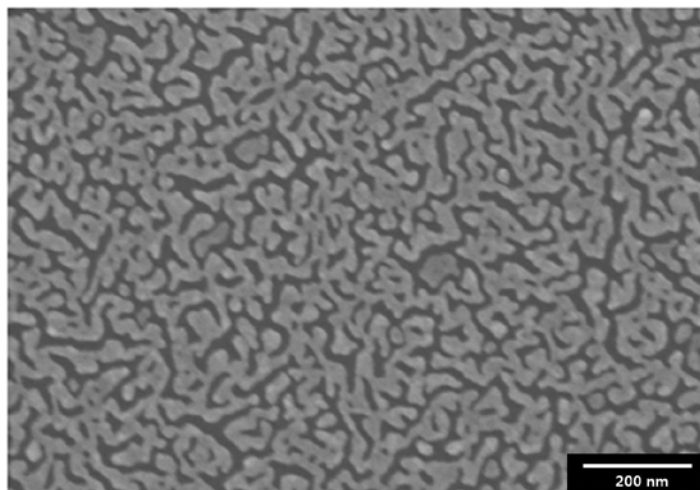
Figure 4-26. FE-SEM images of the 5 nm (a) Au/SiO₂ and (b) Ag/SiO₂ samples after 500 W Ar plasma treatment for 30 min.



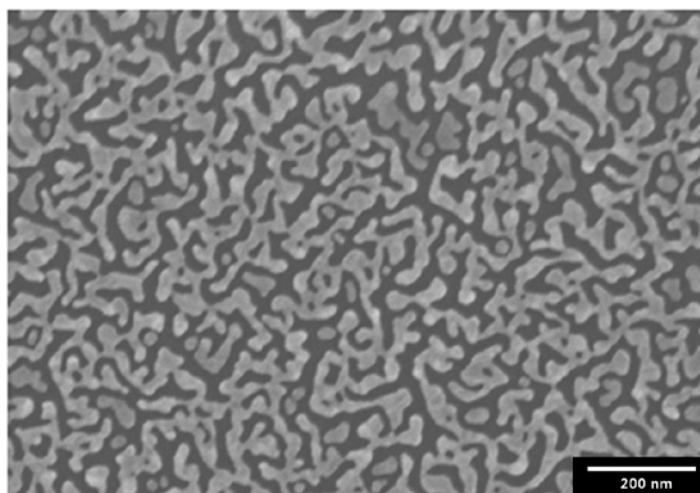
(a)



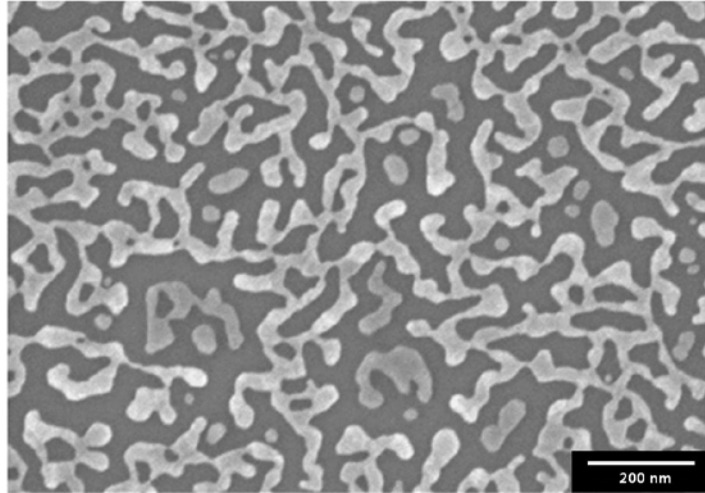
(b)



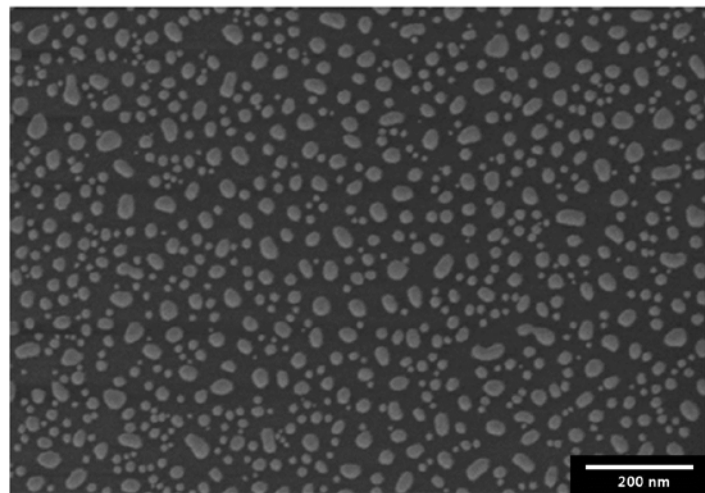
(c)



(d)

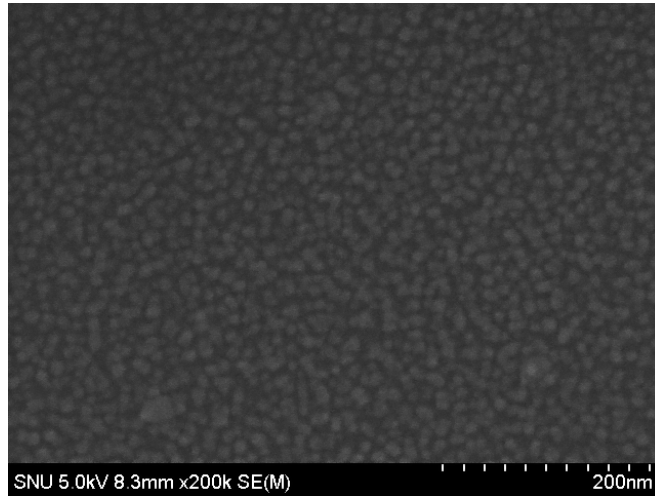


(e)

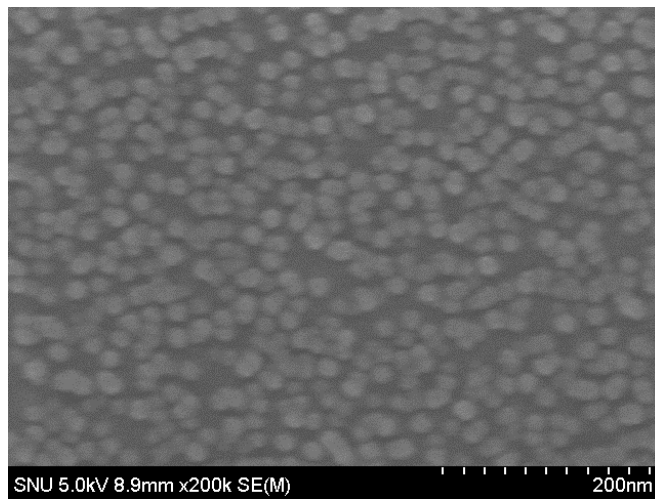


(f)

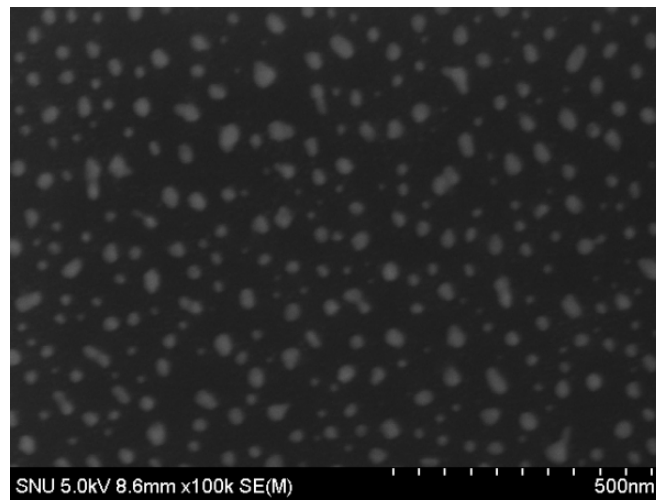
Figure 4-27. FE-SEM images of Au films after the 750 W Ar plasma treatment for different times: (a) as-deposited film, (b) 1 min, (c) 2 min, (d) 3 min, (e) 5 min, and (f) 30 min. Note that (f) has a different scale bar.



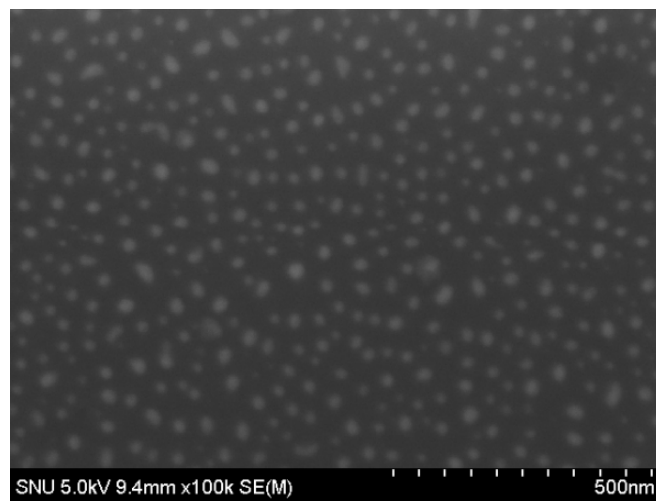
(a)



(b)



(c)



(d)

Figure 4–28. FE–SEM images of the 5 nm (a) Si/SiO₂, (b) Ti/SiO₂, (c) Ni/SiO₂ and (d) Co/SiO₂ samples after Ar plasma treatment for 2 hours using substrate bias. Note that (c) and (d) has a different scale bar with (a) and (b).

5. Conclusion

The research about metal nanoparticle arrays produced by plasma-induced dewetting which is the new synthesizing method for metal nanoparticle array was conducted. Various metal nanoparticle arrays (Cu, Au, Ag, Si, Ni, Co, Ti) were successfully produced at the low temperature (430 K ~ 653 K). The polymer as well as SiO₂ could be used as substrate of metal nanoparticle arrays.

The mechanism of the plasma-induced dewetting was discussed. The dewetting proceeded through heterogeneous hole nucleation, even if the hole nucleation morphology was different with the one induced by thermal annealing. The holes on the plasma treated sample are nucleated in all grain boundaries and their distance is exactly same as grain size while thermally annealed sample has the holes which are sparse and separated by distances greater than the grain size.

Comparing nanoparticles produced by plasma treatment with thermally annealed nanoparticles, plasma treated particles shows uniform distribution. There are two reasons for this phenomenon

(1) Avoiding Coarsening of the nanoparticles at the low process temperature

In plasma treatment, fully dewetted nanoparticles were synthesized at the low process temperature (< 450 K). However, in thermal annealing, fully dewetted nanoparticles were produced at 773 K. At higher temperatures, when the coarsening process becomes dominant, the uniformity of nanoparticles decreases.

(2) Uniformly distributed holes on the surface

The hole nucleation and growth could proceed uniformly during the plasma treatment because a much larger number of holes was formed in plasma, and it resulted in the uniformly distributed nanoparticles.

During plasma-induced dewetting, the oxidation of the nanoparticles occurred less, and nanoparticles less diffused into the substrate than during the thermal annealing because plasma treatment was conducted at the low temperature. Even at the low temperature, ion bombardment which transfers high energy to the substrate surface atoms made dewetting possible.

The uniformity of Cu nanoparticle arrays formed by plasma-induced dewetting was controlled by varying the plasma parameters. The effects of pressure, substrate bias voltage, and applied RF power on the uniformity of nanoparticle arrays were investigated. It was found that uniform nanoparticle arrays were produced when hole generation was increased by using a high ion bombardment energy. When a high amount of energy is transferred to the substrate, a large number of holes are generated uniformly on the substrate, and the isolation of the film proceeded uniformly with the so-called “percolating” structure. On the other hand, when a low amount of energy is transferred to the substrate, a much smaller number of holes are generated on the surface, resulting in non-uniform dewetting.

6. References

1. S. Maenosono, T. Okubo and Y. Yamaguchi, *J. Nano. Res.* 5, 5 (2003)
2. S. H. Sun and C. B. Murray, *J. Appl. Phys.* 85, 4325 (1999)
3. A. V. Malko, A. A. Mikhailovsky, M. A. Petruska, J. A. Hollingsworth, H. Htoon, M. G. Bawendi and V. I. Klimov, *Appl. Phys. Lett.* 82, 1303 (2002)
4. M. I. Baraton and L. Merhari, *J. Nano. Res.* 6, 107 (2004)
5. S. Ludy, L. Chitu, M. Jergel, E. Majkova, P. Siffalovic, A. P. Caricato, A. Luches, M. Martino, R. Rella and M. G. Manera, *Vacuum* 86, 590 (2010)
6. G. H. Chan, J. Zhao, E. M. Hicks, G. C. Schatz and R. P. V. Duyne, *Nano Lett.* 7, 1947 (2007)
7. M. D. Susman, Y. Feldman, A. Vaskevich and I. Rubinstein, *Chem. Mater.* 24, 2501 (2012)
8. W. Zhou, Z. Han, J. Wang, Y. Zhang, Z. Jin, X. Sun, Y. Zhang, C. Yan and Y. Li, *Nano Lett.* 6, 2987 (2006)
9. S. Y. Li, C. Y. Lee and T. Y. Tseng, *J. Cryst. Growth* 247, 357 (2003)
10. S. Y. Li, P. Lin, C. Y. Lee and T. Y. Tseng, *J. Appl. Phys.* 95, 3711 (2004)
11. S. W. Boettcher, J. M. Spurgeon, M. C. Putnam, E. L. Warren, D. B. Turner–Evans, M. D. Kelzenberg, J. R. Maiolo, H. A. Atwater and N. S. Lewis, *Science* 327, 185 (2010)

12. J. Arbiol, B. Kalache, P. R. iCabarrocas, J. R. iMorante and A. F. Morral, *Nanotechnology* 18, 305606 (2007)
13. J. Arbiol, A. iMorral, S. Estrade, F. Peiro, B. Kalache, P. R. iCabarrocas and J. R. iMorante, *J. Appl. Phys.* 104, 064312 (2008)
14. A. K. Gangopadhyay, H. Krichna, C. Favazza, C. Miller and R. Kalyanaraman, *Nanotechnology* 18, 485606 (2007)
15. Z. Liu, C. Lee, V. Narayanan, G. Pei and E. C. Kan, *EEE Trans. Elect. Dev.* 49, 1606 (2002)
16. Z. Liu, C. Lee, V. Narayanan, G. Pei and E. C. Kan, *EEE Trans. Elect. Dev.* 49, 1614 (2002)
17. J. Mizsei. *Sens. Actuators B* 15, 328 (1993)
18. L. Armelao, D. Barreca, G. Bottaro, A. Gasparotto, S. Gross, *Coord. Chem. Rev.* 250, 1294 (2006)
19. H. Baker, H. Okamoto, S. D. Henry, G. M. Davidson, M. A. Fleming, L. Kacprzak and H. F. Lampman, *ASM Handbook* (ASM International, Ohio, 1987) vol. 3, pp. 2
20. P. A. Peterson, Z.J. Radzimski, S.A. Schwalm and P.E. Russell, *J. Vac.Sci. Technol.* 10, 3088 (1992)
21. M. L. Grilli, D. Ristau, M. Dieckmann and U. Willamowski, *Appl. Phys. A.* 71, 71 (2000)
22. M. Khan, G. Han, S.B. Bollepalli and F. Cerrina, *J. Vac. Sci. Technol.* B17, 3426 (1999)
23. T. Kitayama, K. Itoga, Y. Watanabe and S. Uzawa, *J. Vac. Sci. Technol.* B18, 2950 (2000)
24. L. Yang and J.W. Taylor, *J. Vac. Sci. Technol.* B19, 129 (2000)

25. R. F. Service, *Science* 293, 785 (2001)
26. F. S. Chien, C.L. Wu, Y.C. Chou, T.T. Chen, S. Gwo and W.F. Hsieh, *Appl. Phys. Lett.* 75, 1 (2000)
27. E. S. Snow, D. Park and P.M. Campbell, *Appl. Phys. Lett.* 69, 269 (1996)
28. C. F. Quate, *Surface Science* 386, 259 (1997)
29. S. Y. Chou, P.R. Krauss and P.J. Renstrom, *Appl. Phys. Lett.* 67, 3114 (1995)
30. B. H. Lee, Y.H. Cho, H. Lee, K.D. Lee, S.H. Kim and M.M. Sung, *Adv.Mater.* 19, 1714 (2007)
31. K. Oh, B.H. Lee, J.K. Hwang, H.Lee, K.H. Lee, S. Im and M.M. Sung, *Small* 5, 558 (2009)
32. L. Qian, S. Zhai, Y. Jiang and B. Das, *J. Mater. Chem.* 22, 4932 (2012)
33. X.M. Zhao, Y. Xia and G.M. Whitesides, *Adv. Mater.* 8, 837 (1996)
34. Y. Liu, C. Lor, Q. Fu, D. Pan, L. Ding, J. Liu and J. Lu, *J. Phys. Chem. C* 114, 5767 (2010)
35. J. Li, K. Kamata, S. Watanabe and T. Iyoda, *Adv. Mater.* 19, 1267 (2007)
36. J. Y Kwon, T. S. Yoon and K. B. Kim, *J. Appl. Phys.* 93, 3270 (2003)
37. J. Trice, D. Thomas, C. Favazza, R. Sureshkumar and R. Kalyanaraman, *Phys. Rev. B.* 75, 235439 (2007)
38. V. A. Shchukin and D. Bimberg, *Rev. Mod. Phys.* 71, 1125 (1999)

39. J. J. Lee, Surf. Coat. Tech. 169, 353 (2003)
40. A. Vrij, Discuss. Fara. Soc. 42, 23 (1966)
41. A. W. Rucker, Nature 16, 331 (1877)
42. J. Israelachvili, Intermolecular surface forces (Academic, N. Y, 1992), 2nded.
43. S. Dietrich, Phase Transition and Critical Phenomena, edited by C. Domb and J. L. Lebowitz (Academic, London, 1988), Vol. 12.
44. K. Jacobs and S. Herminghaus, Langmuir 14, 965 (1998).
45. F. Spaepen, Mech. Phys. Solids 44, 675 (1996)
46. W. W. Mullins, J. Appl. Phys. 30, 77 (1959)
47. D. J. Srolovitz and S. A. Safran, J. Appl. Phys. 60, 247 (1986)
48. P. R. Gadkari, A. P. Warren, R. M. Todi, R. V. Petrova and K. R. Coffey, J. Vac. Sci. Tech. A 23, 1152 (2005)
49. M. A. Lieberman and A. J. Lichtenberg, Principles of plasma Discharges and Materials Processing (second edition, John Wiley & Sons, Inc. 2005)
50. E. Sutter and P. Sutter, Nanotechnology 17, 3724 (2006)
51. H. Brune, M. Giovannini, K. Bromann and K. Kern, Nature 394, 451 (1998)
52. C. Teichert, M. G. Lagally, L. J. Peticolas and J. C. Bean, Phys. Rev. B 53, 16334 (1996)
53. N. T. Gladkikh, R. Neidermayer and K. Spiegel, Phys. Status Solidi. 15, 181 (1966)
54. G. Reiter, Phys. Rev. Lett. 68, 75 (1992)

55. J. W. Strutt, Proc. London Math. Soc. 10, 4 (1878)
56. D. T. Danielson, D. K. Sparacin, J. Michel and L. C. Kimerling, J. Appl. Phys. 100, 083507 (2006)
57. G. Fantner, Atomic Force Microscopy, Advanced Bioengineering Methods Laboratory, Ecole Polytechnique Federale De Lausanne
58. M. A. Lieberman and A. K. Lichtenberg, Principles of Plasma Discharges and Materials Processing Vol. 1 John Wiley & Sons, Inc. Hoboken New jersey, p. 171 – 172 (2005)
59. Y. Yamamura and H. Tawara, Atomic Data and Nuclear Data Table 62, 149–253 (1996).
60. K. K. Choi, J. H. Yun and S. W. Rhee, Thin Solid Films 429, 255 (2003)
61. T. Fujikawa, T. Yoshikawa, T. Ohnishi and T. Sato, Japan. J. Appl. Phys. 40, 2191 (2001)
62. Q. T. jiang and K. Smekalin, Advanced Metallization Conf. in 1998 ed G. S. Sandhu, H. Koerner, M. Murakami, Y. Yasuda and N. Kobayashi (Warrendale, PA: Materials Research Society) pp 209–15 (1998)
63. J. D. Carey, L. L. Ong and S. R. P. Silva, Nanotech. 14, 1223 (2003)
64. S. Lucas and P. Moskovkin, Thin Solid Films 518, 5355 (2010)

65. U. Diebold, J. M. Pan and T. E. Madey, Phys. Rev. B 47, 3868 (1993)
66. L. Stolt and F. M. D' Heurle, Thin Solid Films 189, 269 (1990)
67. E. A. Brandes and G. B. Brook, Smithells Metals Reference Book, 7th ed.

초록

플라즈마를 이용한 디웨팅을 이용하여 금속 나노 분말 어레이를 만드는 방법을 새로 개발하였다. 구리, 은, 금, 실리콘, 니켈, 코발트, 티타늄과 같은 다양한 금속 박막을 금속 나노 분말 어레이로 변환시키는 공정을 저온에서 성공적으로 진행하였다. 또한 플라즈마를 이용한 디웨팅이 어떠한 방식으로 진행되는지 그 메커니즘 역시 밝혔다. TEM과 SEM 사진을 비교하여 분 디웨팅이 헤테로지니어스 홀 뉴클리에이션으로 진행된다는 사실을 알아냈다.

플라즈마를 이용하여 제작된 나노 분말 어레이는 기존의 열처리 방법으로 제작된 것 보다 더욱 균일하게 분포되어 있었다. 그 이유는 플라즈마 공정에서는 낮은 공정온도가 나노 분말들의 조대화를 막고, 나노 분말 형성의 균일도를 결정하는 원인이 되는 홀의 생성이 박막 표면에서 균일하게 일어나기 때문이다.

오제 전자 분석을 통하여 플라즈마를 이용하여 생성된 나노 분말이 산화가 덜 일어난다는 사실을 밝혀내었다. 그 이유는 공정온도가 낮기 때문인데, 이렇게 낮은 공정온도에서도 금속 필름 표면의 분자가 이동할 수 있는 이유는 플라즈마 내의 이온이 필름 표면 분자에 높은 에너지를 전달하기 때문이다.

나노 분말 어레이들의 균일도를 플라즈마에서 조절할 수 있는 변수를 이용하여 조절하였다. 플라즈마 밀도와 전자 온도를 조절하는 방식으로는 공정압력과 인가 파워를 바꾸는 방식을 이용하였고, 쉬스 전압을 조절하는 방식으로는 기판에 직접적인 RF 바이어스를 거는 방식을 채택하였다. 이러한 실험으로 기판에 강한 에너지가 입사하였을 때 홀의 생성이 균일하면서

많아지고 따라서 균일한 나노 분말 어레이가 나온다는 사실을 밝혀내었다. 반대로 낮은 에너지를 기판에 입사시킨 경우는, 박막 표면에 생성되는 홀의 개수가 상대적으로 적고 불균일하기 때문에 생성되는 나노 분말 어레이 역시 불균일하였다.

감사의 글

2004년 서울대학교를 처음 들어온 날이 엇그제 같은데, 벌써 9년이라는 시간이 지났습니다. 뒤돌아보면 힘들고 아쉬운 일도 많았지만 그럴 때 마다 여러분들의 도움 속에서 앞으로 나아갈 수 있었다고 생각합니다. 이 지면을 빌어 모두에게 감사의 말씀을 드리고 싶습니다.

먼저 학부를 마친 저를 연구실에 받아주시고 5년동안 지도해주신 이정중 교수님께 감사드립니다. 인자하신 성품으로 항상 저희의 의견을 존중해주시고, 연구에 관해서나 인생에 관해서나 모든 방면에 있어서 진실된 충고와 격려를 해주신 교수님을 저의 지도교수님으로 모실 수 있어서 지난 시간 동안 큰 영광이 되었습니다. 박사과정을 하면서 얻을 수 있는 가장 큰 배움은 지식이 아니라 스스로 새로운 일을 해나갈 수 있는 능력이라고 생각합니다. 교수님의 가르침이 아니었다면, 혼자 생각하고 계획하고 또한 그것을 실행해 나가는 능력을 기를 수 없었을 것입니다.

또한 논문 심사위원장을 맡아주시면서 따뜻한 말씀으로 지도를 해주신 강신후 교수님과 훌륭한 수업과 인자하신 성품으로 재료에 대한 지식과 연구에 관하여 가르쳐주시고 논문 심사위원까지 맡아주신 박은수 교수님께도 감사드립니다. 그리고 군산에서 플라즈마에 관한 깊은 식견으로 항상 저희 연구실에 큰 도움과 가르침을 주시는 주정훈 교수님과 다양한 공동연구로 저의 식견을 넓혀주시고 많은 가르침을 주신 한양대학교의 정진욱 교수님께도 진심으로 감사의 말씀을 드립니다.

대학원 생활을 하면서 연구실 선배님들이 안계셨다면 지금의 저는 없었을 것입니다. 좋은 연구주제로 저를 챙겨주시고, 또한 후배들을 항상 생각해주는 영훈이형, 입학하자마자 대학원 생활에 대하여 많은 충고와 따뜻한

말씀을 해주셨던 보환이형, 항상 웃음으로 신입생이었던 저를 맞아주셨던 훈이형, 처음으로 실험방법에 대하여 친절하게 알려주시고 논문을 쓰게 해주셨던 희용이형께 감사의 말씀을 전합니다. 오랫동안 옆자리에서 정이 들어 졸업할 때 정말 슬펐던 경희누나, 브레인으로 연구실을 잘 이끌어주셨던 진남이형, 남다른 행동력과 분석력으로 연구실의 주축이셨던 효석이형, 함께 연구하며 도움을 받았던 동훈이형에게도 감사의 인사를 드립니다. 그리고 항상 재치있고 인자한 모습으로 웃음을 잃지 않으시는 성만이형께도 언제나 주님의 은총이 함께하길 바랍니다. 또한 먼저 졸업하신 항상 웃으셨던 소미누나, 저의 소중한 동기 민우형, 아프셨지만 남다른 열정으로 실험하셨던 필주형도 항상 건강하고 하시는 일 모두 승승장구 하시길 바랍니다. 그리고 저에게 기타를 가르쳐주고 학부 동기로서 든든한 친구가 되어주었던 태운이에게도 감사의 말을 전하고 싶습니다.

지금 연구실의 정신적 지주이며 스마트하시고 축구신동이시며 저 뿐만이 아니라 모든 연구실 동료들에게 아낌없는 도움을 주시는 동수형! 연구실의 기둥 중 하나로 언제나 주님 안에서 생활하시는 정말 부러운 따뜻한 마음의 소유자 신영이형! 제 연구실 생활 5년간 항상 연구실의 중추였으며 저를 포함한 후배들에게 언제나 따뜻하게 대해준 원혁이형! 냉철하고 이성적이지만 인간적으로도 친근한 우리 창희! 저와 함께 연구를 하는, 언제나 모든 일에 최선을 다하는 맑은 마음의 소유자 한주형! 이번에 저와 함께 졸업하는 사려 깊은, 그리고 하는 일에 빈틈이 없는 모태 부장님 동희형! 재밋고 꼼꼼하고 배려적이고 열정적인 정말 배울게 많은 석진이형! 모두들 사랑하고 감사하고 언제나 자신의 분야에서 승리하시길 바랍니다.

박사과정을 하면서 한양대에서 저와 함께 연구에 대하여 토론해 주시고 플라즈마에 대하여 많은 가르침을 주신 이효창 박사님 (효창이형~)께도 감사의 말씀을 드립니다. 그리고 20대를 항상 함께 보내며 정신적으로 육체적으로 언제나 도움을 주었던 나의 가장 절친한 친구들 현기와 홍찬이

너무 감사 드리고, 내가 별명을 지어준 것이 평생동안 가게 생긴 우리 나나 지훈이, 같은 성씨인 04학번 브라더 수빈이, 참 착하고 따뜻하고 머리 큰 우리 태훈이, 쭈노~라고 나를 불러주면서 항상 웃겨주었던 배후나짱, 혀로 냉면을 끊어먹는 촌테레 혀도, 간지의 대명사 하지만 술먹으면 눈물나는 간지노님, 수영 선배이자 따뜻한 마음으로 절 많이 도와준, 그리고 카톡방에서 수빈이와 간지노를 까는 독설로 절 항상 웃겨주는 쿤동이, 저와 함께 일찍 결혼한 우리 근하, 항상 물심양면으로 저를 도와주었던 재간둥이 만능 휴머노이드이자 겨울에도 추위를 타지 않는게 신기한 동민이, 그 전에는 몰랐는데 천재라는걸 대학교 3학년때 깨달은, 뭔가 덤병대는듯 하지만 사실은 모든면에서 완벽한 지환이, 엄청난 연구성파로 미래의 빛이 될 고등학교 시절부터 대학까지 친구인 참 정이 많은 덕황이, 요즘 아파서 걱정이지만 조만간 건강해지리라 믿어 의심치 않는 자규, 학부생활 동안 함께한 04학번 동기들에게 진심으로 감사드립니다. 그리고 학부 동안 동문회에서 동고동락한 민수형, 성우형, 성곤이형, 기웅이형, 인혁이형, 세준이형, 용환이, 대진이, 수영이, 재엽이, 민호, 그리고 고등학교 시절부터 친한 친구였던 오랫동안 보지 못했지만 항상 보고 싶은 우리 현석이. 서울대 힙합동아리 bounce factory, 결혼식 축하까지 불러준, 항상 나를 도와주었던 나의 절친 보라에게도 감사의 인사를 드립니다.

언제나 가족으로써 저를 사랑으로 감싸주셨던, 주님 곁에서 저를 지켜봐 주시는 할아버님, 외할아버님. 늘 격려와 성원을 주시며 도움을 주시는 우리 친가, 외가 식구들에게 진심으로 감사드립니다.

마지막으로 저를 낳아주시고 길러주시며 언제나 어디서나 무슨 일이 생기거나 항상 저의 편이 되어주셨고 주시는, 세상 그 무엇보다 소중한 우리 어머니, 아버지 그리고 동생 순영이. 사위인 저를 항상 아들같이 대해주시며 존중해 주시고, 편안함과 따뜻함을 느끼게 해주시는 우리 사랑하는 장모님 장인어른, 꿈 같은 인연으로 저의 동반자가 되어주고 항상 저를 웃게 해주며

내 인생의 의미이고 앞으로 미래의 나를 만들어 줄 영원한 진행형 사랑 우리
은혜, 항상 곁에 살피시어 저희 가족을 화목으로 채워주시는 하나님께 감사의
말씀과 더불어 이 논문을 바칩니다.

2013년 새벽 빛을 받으며

권순호